



New shock microstructures in titanite (CaTiSiO_5) from the peak ring of the Chicxulub impact structure, Mexico

Nicholas E. Timms¹ · Mark A. Pearce² · Timmons M. Erickson^{1,3} · Aaron J. Cavosie¹ · Auriol S. P. Rae^{4,5} · John Wheeler⁶ · Axel Wittmann⁷ · Ludovic Ferrière⁸ · Michael H. Poelchau⁵ · Naotaka Tomioka⁹ · Gareth S. Collins⁴ · Sean P. S. Gulick¹⁰ · Cornelia Rasmussen¹⁰ · Joanna V. Morgan⁴ · IODP-ICDP Expedition 364 Scientists

Received: 16 November 2018 / Accepted: 19 March 2019
© Springer-Verlag GmbH Germany, part of Springer Nature 2019

Abstract

Accessory mineral geochronometers such as apatite, baddeleyite, monazite, xenotime and zircon are increasingly being recognized for their ability to preserve diagnostic microstructural evidence of hypervelocity-impact processes. To date, little is known about the response of titanite to shock metamorphism, even though it is a widespread accessory phase and a U–Pb geochronometer. Here we report two new mechanical twin modes in titanite within shocked granitoid from the Chicxulub impact structure, Mexico. Titanite grains in the newly acquired core from the International Ocean Discovery Program Hole M0077A preserve multiple sets of polysynthetic twins, most commonly with composition planes (K_1) = $\sim \{ \bar{1}11 \}$, and shear direction (η_1) = $<110>$, and less commonly with the mode $K_1 = \{ 130 \}$, $\eta_1 = \sim <522>$. In some grains, $\{ 130 \}$ deformation bands have formed concurrently with the deformation twins, indicating dislocation slip with Burgers vector $\mathbf{b} = <341>$ can be active during impact metamorphism. Titanite twins in the modes described here have not been reported from endogenically deformed rocks; we, therefore, propose this newly identified twin form as a result of shock deformation. Formation conditions of the twins have not been experimentally calibrated, and are here empirically constrained by the presence of planar deformation features in quartz (12 \pm 5 and \sim 17 \pm 5 GPa) and the absence of shock twins in zircon (< 20 GPa). While the lower threshold of titanite twin formation remains poorly constrained, identification of these twins highlight the utility of titanite as a shock indicator over the pressure range between 12 and 17 GPa. Given the challenges to find diagnostic indicators of shock metamorphism to identify both ancient and recent impact evidence on Earth, microstructural analysis of titanite is here demonstrated to provide a new tool for recognizing impact deformation in rocks where other impact evidence may be erased, altered, or did not manifest due to generally low (< 20 GPa) shock pressure.

Keywords Titanite · Shock metamorphism · Mechanical twinning · Dislocation slip system · Meteorite impact · EBSD

Introduction

Identifying and dating impacts are essential to understand their role in key processes in Earth history, such as mass extinctions (e.g. Hildebrand et al. 1991) and even the proposed relation to the onset of plate tectonics (O’Neill et al.

2017). Recent crystallographic and microstructural studies of datable accessory minerals such as zircon (e.g. Moser et al. 2011; Timms et al. 2012; Erickson et al. 2013; Cavosie et al. 2016a, 2018a; Crow et al. 2018), monazite (e.g. Erickson et al. 2016, 2017a), baddeleyite (e.g. Darling et al. 2016; Timms et al. 2017a; White et al. 2018), and xenotime (Cavosie et al. 2016b) have greatly expanded the potential to both recognize and date impact events (e.g. Erickson et al. 2017b). Titanite (CaTiSiO_5) is a widely utilized U–Pb geo- and thermochronometer that occurs in a broad range of potential target rock compositions (Frost et al. 2001), including metamorphic, sedimentary, and felsic to mafic igneous rocks. We report a detailed electron backscatter diffraction (EBSD) microstructural study of impact deformation

Communicated by Daniela Rubatto.

The members of “IODP-ICDP Expedition 364 Scientists” are mentioned in the Acknowledgements section.

✉ Nicholas E. Timms
n.timms@curtin.edu.au

Extended author information available on the last page of the article

in titanite, focusing on samples of shocked granitoid from the 2016 International Ocean Discovery Program (IODP)-International Continental scientific Drilling Program (ICDP) Expedition 364, that drilled the peak ring of the 200-km-wide Chicxulub impact structure off the coast of the Yucatán Peninsula (Morgan et al. 2017). We further demonstrate how these features can be distinguished from deformation of titanite due to endogenic tectonic stresses.

Titanite crystallography, microstructure, and deformation

Titanite, formerly known as sphene until renamed by the International Mineralogical Association (Hey 1982), has the nominal formula CaTiSiO_5 , with an atomic structure comprising chains of octahedral sixfold Ti and fourfold Si, with Ca occupying a sevenfold site (Higgins and Ribbe 1976; Speer and Gibbs 1976). At ambient pressure and temperature, titanite is monoclinic, and belongs to the space group family $\text{P}2_1/a$ (Speer and Gibbs 1976; Taylor and Brown 1976). Above 496 °K (223 °C), displacements of adjacent octahedral Ti chains define a transition to an intermediate structure (Kunz et al. 1996). Above 825 °K (552 °C), or above ~3.5 GPa at room temperature, further modification of the structure results in an orthorhombic A2/a symmetry that accommodates a volume reduction of 5.1% (Salje et al. 1993; Kunz et al. 1996; Angel et al. 1999). Titanite melts at >1380 °C (Hayward and Cecchetto 1982).

Titanite has good cleavage along {110}, and can form simple growth twins parallel to (100) (Deer et al. 1982). Two sets of symmetrically equivalent, polysynthetic lamellar mechanical (deformation) twins in titanite were first reported by Mügge (1889) and have since been documented in rocks affected by high-strain rates. Deformation twins were reported in samples affected by 0.5–0.8 GPa pressure during nuclear tests (Borg 1970), and were subsequently produced in laboratory experiments at 0.8 GPa (Borg and Heard 1972). The twin mode for deformation twins was defined as $K_1 = \sim\{221\}$, $\eta_1 = <110>$, where K_1 = twinning (or composition) plane and η_1 = shear direction (Borg 1970). With a critically resolved shear stress of ~0.13 GPa at 500 °C, $\sim\{221\}<110>$ twinning can occur in titanite at typical endogenic tectono-metamorphic conditions (Borg and Heard 1972; Bonamici et al. 2015).

Titanite can also undergo dislocation creep (Müller and Franz 2004; Bonamici et al. 2015) and dynamic recrystallization (Papapavlou et al. 2017) in tectono-metamorphic settings. Crystal-plastic deformation of titanite is not well studied. Dislocations with Burgers vectors (\mathbf{b}) = [100], [011] and [011] have been reported in titanite at eclogite facies, and easy glide of dislocations with $\mathbf{b} = \frac{1}{2}<011>$ that

is predicted to occur in the A2/a phase (Müller and Franz 2004). Recrystallised subgrains with low- and high-angle boundaries have also been reported in tectonically deformed titanite (Bonamici et al. 2015; Papapavlou et al. 2017; Kirkland et al. 2018).

Titanite grains have been experimentally dynamically shocked to 59 GPa (Deutsch and Schärer 1990). However, the resulting microstructures were not characterized in detail. Previously reported titanite microstructures in naturally shocked rocks that did not involve quantitative approaches have been described simply as ‘sub-planar fractures’ (e.g. Koeberl et al. 1996; Papapavlou et al. 2018), ‘planar fractures’ and ‘mechanical twinning’ (Biren and Spray 2011). In breccia from the Ries crater, Germany, Chao (1968) reported weakly developed planar features and misoriented mosaic textures, whereas Abadian (1972) reported dominant cleavage along (111) and (110), less common cleavage in an irrational plane $\parallel(552)$, and fine (1–2 μm wide) planar elements parallel to the {010} zones. Electron backscatter diffraction analysis of titanite in target rocks from the Sudbury impact structure, Canada, and Vredefort impact structure, South Africa, revealed crystal-plastic deformation, lamellar twins with ~74°/ <102> host-twin disorientation axes, and neoblasts (Papapavlou et al. 2018). However, twins identified in these studies have not been indexed. Until now, no studies have focused on quantitatively distinguishing the style of deformation features that form in titanite in tectonic stress regimes from those that form during impact events, which is the focus of this study.

Geological background and samples

This study investigates titanite from the ~66 Ma, 200-km Chicxulub impact structure in the Gulf of Mexico and Yucatán Peninsula, which is widely reported to have caused the K-Pg mass extinction (Hildebrand et al. 1991; Schulte et al. 2010; Renne et al. 2013). It is one of the three largest known terrestrial impact structures (Grieve and Therriault 2000) and contains a well-preserved peak ring (Fig. 1) (Morgan et al. 1997; Gulick et al. 2008, 2013; Morgan et al. 2016; Riller et al. 2018). In 2016, IODP-ICDP Expedition 364 drilled core from Hole M0077A (21° 27.009'N, 89° 56.962'W), which penetrated the peak ring (Morgan et al. 2017) (Fig. 1). Recovered lithologies include a section of shocked Paleozoic granitoid basement rocks from depths of 747–1335 metres below sea floor (mbsf) that contain pre-impact mafic and felsic dike lithologies as well as intercalations of impact breccia and impact melt rocks (Fig. 1) (Morgan et al. 2017).

The granitic target rocks are coarse grained and primarily composed of alkali feldspar, quartz, plagioclase, minor biotite, and accessory muscovite, apatite, titanite, epidote, magnetite, ilmenite, and zircon (Gulick et al. 2017; Morgan

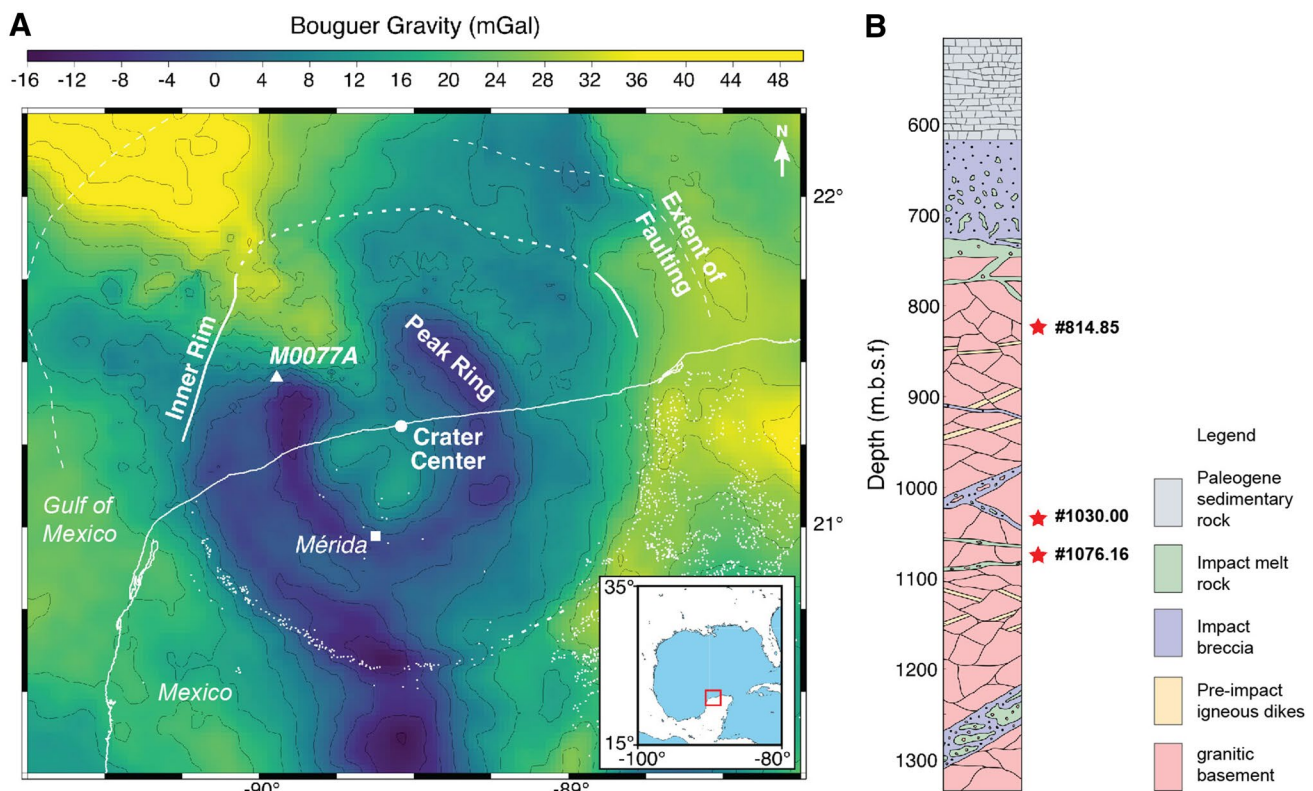


Fig. 1 **a** Gravity anomaly map of the Chicxulub impact structure showing traces of various morphological features of the buried crater (dashed lines), location of Hole M0077A, and sinkholes (cenotes) (white dots), and present-day coastline (solid white line). **b** Schematic

core log of Hole M0077A showing the distribution of lithologies and locations of samples used in this study. After Morgan et al. (2016) and Gulick et al. (2013)

et al. 2017; Schmieder et al. 2017). Most quartz grains contain multiple decorated planar deformation features (PDFs), planar fractures (PFs), and feather features (FFs) (Fig. 2) (e.g. Ferrière et al. 2017; Gulick et al. 2017; Morgan et al. 2017; Rae et al. 2017; Zhao et al. 2017; Rae 2018). Preliminary universal stage (U stage) analysis of PDF orientations in shocked quartz constrains the bulk shock pressure of rocks in the core to $\sim 12 \pm 5$ – 17 ± 5 GPa (Rae et al. 2017; Feignon et al. 2018; Rae 2018). Titanite grains up to 2 mm long occur as inclusions within all major phases of the granitic rocks, including shocked quartz, and are often spatially associated with and/or include other accessory phases, such as zircon and apatite (Figs. 2, 3).

Analytical methods

Samples and approach used in this study

Titanite grains and associated phases were characterized via optical microscopy, backscattered electron (BSE) imaging, and EBSD mapping in thin sections of three shocked granite

core samples from Hole M0077A (364-77-A-121-R-1-75-77, 364-77-A-204-R-1-7-9, and 364-77-A-219-R-1-22-24) from depths of 814.85, 1030.00, and 1076.16 mbsf, respectively (Figs. 2, 3; Table 1). The samples are referred to throughout this study by these depths with # prefix (Table 1). Modes of twinning in titanite identified from EBSD data were determined via analysis of the host–twin crystallographic orientation relationships. A MATLAB script was used to determine the directions defining 180° misorientation relationships, which correspond to either the twinning direction of shear (η_1) or the pole to the compositional plane (twin plane, K_1) (Christian and Mahajan 1995; Erickson et al. 2016). Finally, twins were indexed using geometric considerations (Christian and Mahajan 1995) combined with the traces of twin lamellae on EBSD maps. The geometry of low-angle lattice distortions associated with deformation bands seen in EBSD data was analysed, including automated calculation of the weighted Burgers vector (Wheeler et al. 2009).

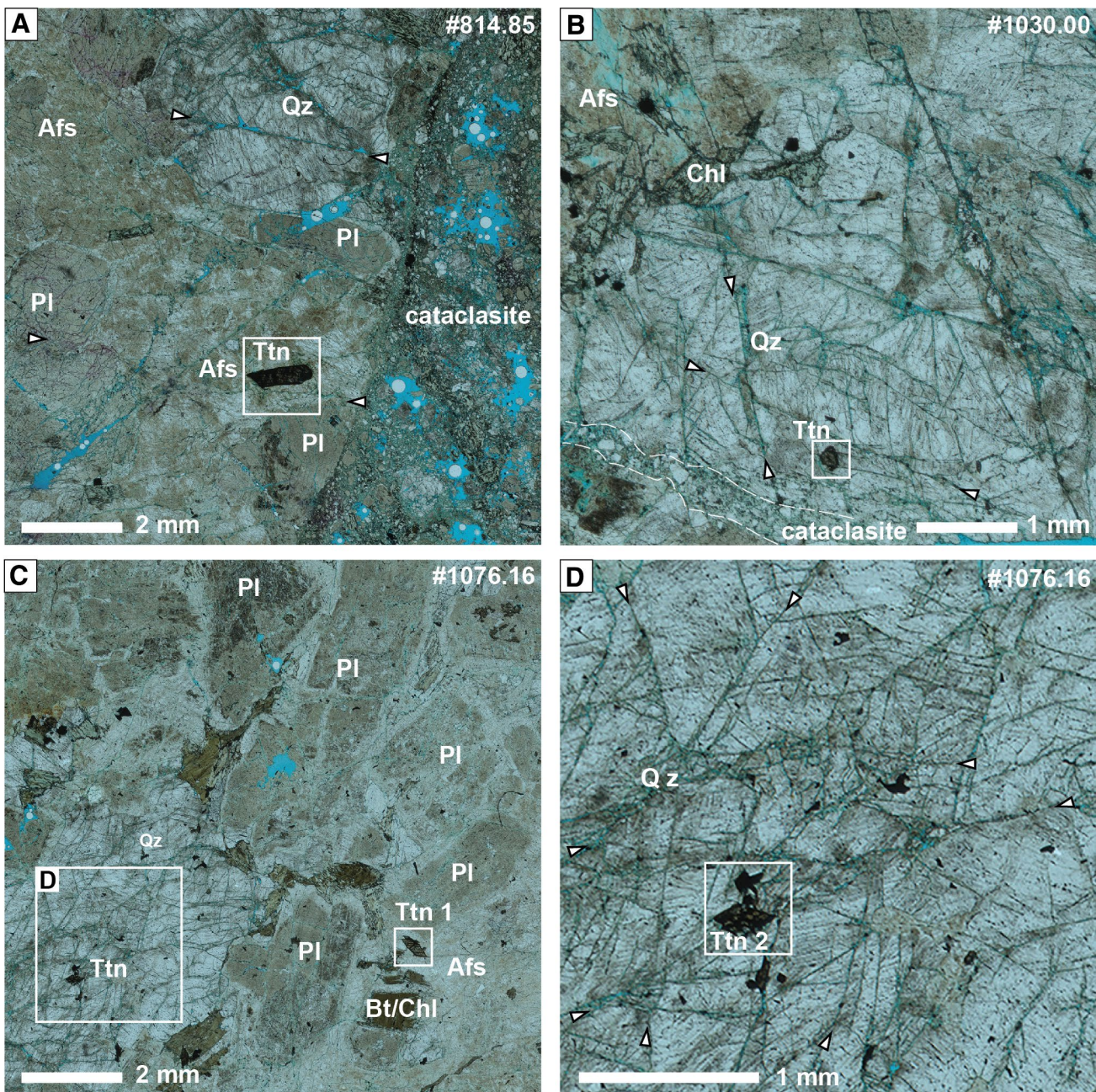


Fig. 2 Optical photomicrographs of the samples used in this study. Mineral abbreviations after Whitney and Evans (2009) include *Qz* quartz, *Afs* alkali feldspar, *Pl* plagioclase, *Ttn* titanite, *Chl* chlorite, and *Bt* biotite. **a** #814.85. **b** #1030.00. **c** #1076.16. **d** Region of interest in #1076.16 shown by white box in **c**. White arrows annotate significant fracture orientations. Samples were impregnated with blue epoxy prior to thin sectioning to enable the porosity to be visualized. Plane-polarized light images

est in #1076.16 shown by white box in **c**. White arrows annotate significant fracture orientations. Samples were impregnated with blue epoxy prior to thin sectioning to enable the porosity to be visualized. Plane-polarized light images

Scanning electron microscopy and electron backscatter diffraction mapping

Prior to scanning electron microscopy, thin sections were polished progressively with diamond paste to 0.5 μm ,

then given a final polish using 0.06- μm colloidal silica in NaOH on a Buehler Vibromet II for 4 h. A thin carbon coat was applied to mitigate charging. Backscattered electron images were collected using a Tescan MIRA3 field emission scanning electron microscope (FE-SEM) in the John

de Laeter Centre at Curtin University. Phases and their crystallographic microstructures were quantified using combined energy-dispersive X-ray (EDX) and electron backscatter diffraction (EBSD) mapping using an Oxford Instruments AZtec system on the Tescan MIRA3 FE-SEM at Curtin University. Data acquisition settings and processing procedures followed those of Timms et al. (2017b) and are detailed in Table 2. EBSD data were processed using the Tango and Mambo modules of Oxford Instruments Channel 5.10 to produce thematic maps and pole figures, respectively.

Determining twin modes from EBSD data

EBSD mapping involves quantification of the crystallographic orientation of phases relative to the sample surface. It is conventional to describe this absolute crystallographic orientation in the x - y - z sample reference frame at a given x - y point on the map as a sequence of three rotations from a reference orientation, known as Euler angles ϕ_1 , Φ , and ϕ_3 (Bunge 1981; Prior et al. 1999). Twins are recognized in EBSD maps as domains with a specific systematic misorientation relationship relative to the host grain. Misorientation is defined as the rotation around an axis by some angle that would bring any two differently orientated crystals into alignment (Wheeler et al. 2001). Due to the symmetry of crystals, multiple misorientation axes are present. Each axis corresponds to a different angular rotation, and all of these orientations describe the relationship between the two domains. The most commonly reported type of misorientation in EBSD data sets is the axis around which the minimum rotation is required for realignment, which is specified as the disorientation (Wheeler et al. 2001). This distinction is important when considering mechanical twinning, where it is conventional to classify twin modes based on rotations around axes where the misorientation angle is 180°, and which may be different to the disorientation.

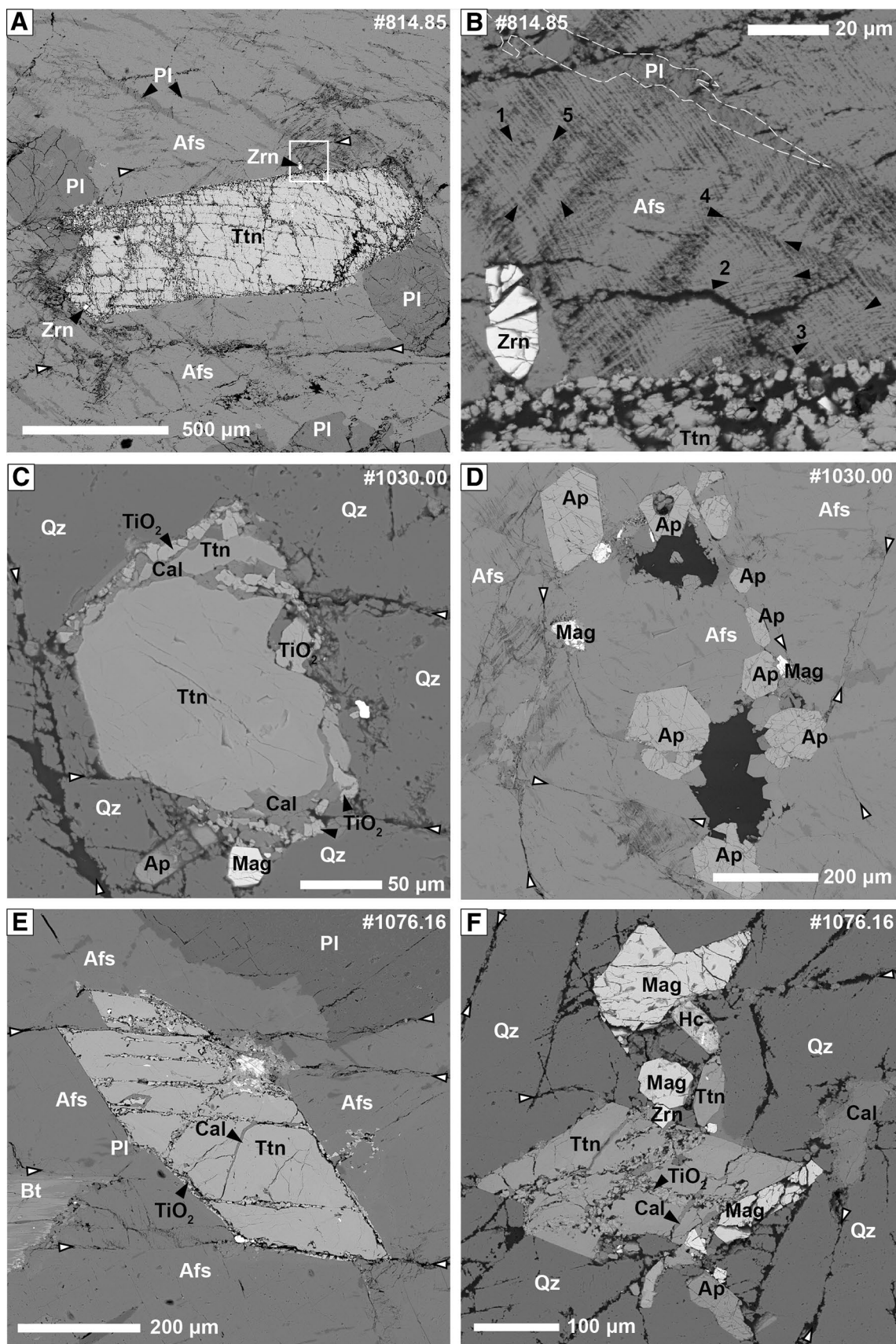
Deformation twins are characterized using one or both of the twinning/composition planes, K_1 , and shear direction, η_1 , which results in 180° misorientation relationships (Christian and Mahajan 1995). Deformation twins can be classified into one of three ways. Type 1 twins have a rational K_1 , the pole to which is a misorientation axis with rotation angle of 180°, and an irrational η_1 . Conversely, type 2 twins have rational η_1 , around which is a misorientation axis with the rotation angle of 180°, and an irrational K_1 , and compound twins are defined by both rational K_1 and η_1 , both of which are misorientation axes with rotations of 180° (Christian and Mahajan 1995). In general, the relationship reported by EBSD software will not have a rotation angle of 180°, as there will usually be a lower angle disorientation relationship. The exceptions to this issue are in triclinic minerals (where there is only one symmetric equivalent) and

compound twins in monoclinic minerals (where there are two symmetric equivalents and, therefore, they must both be components of the twinning). This relationship means it is possible for the disorientation angle/axis to bear no resemblance to K_1 and η_1 for various twin modes in most crystal systems.

A more sophisticated analysis of EBSD data that involved calculating 180° misorientations is required to identify K_1 and η_1 for twinning in monoclinic phases such as monazite (Erickson et al. 2016). A MATLAB script was developed that utilizes Euler angle triplets for two representative data points from the host and adjacent twin domain derived from the EBSD map, crystal unit cell parameters, and Laue group symmetry operators as input parameters (Table 3).

First, the rotation matrix (\mathbf{R}), which describes the orientation relative to a reference orientation, is calculated for each Euler triple (host \mathbf{R}_h , twin \mathbf{R}_t) using equations B2 and B4 of Cho et al. (2005). These can be used to calculate the directions in sample coordinates of particular crystal directions. For our purposes, we require a matrix which describes the rotation from host to twin expressed in crystal coordinates ($\mathbf{R}_m = \mathbf{R}_h^{-1}\mathbf{R}_t$). Since this is in crystal coordinates, we derive rotation matrices for each symmetric equivalent ($\mathbf{R}_m^i = \mathbf{S}_i \mathbf{R}_m$) where \mathbf{S}_i is the i th member of the set of symmetry operators for the Laue class under consideration. The 180° misorientation axes were calculated as angle/axis pairs in Cartesian x - y - z -coordinates (the sample reference frame). These were used to find best-fit crystallographic forms using the dot product of unit vectors, as $\langle hkl \rangle$ or pole to $\{hkl\}$, implementing integer search limits of 4–4 for h , k , and l to yield low-index (rational) best-fit forms. Output data were compiled giving the crystallographic vector with the smallest value normalized to 1 and their corresponding angular deviation from the calculated misorientation axis. The orientation of K_1 , η_1 and S was reconstructed using a stereographic projection, ensuring that the appropriate symmetric variants of K_1 and η_1 were chosen such that its great circle contains the mapped x - y trace of the twins and η_1 .

The K_1 and η_1 components of twin modes were deemed to be rational if angular deviation between the calculated misorientation axis and the best-fit low-index crystallographic form were $< 0.7^\circ$, which is a reasonable value given the mean angular deviation associated with indexing EBSD data points is typically on the order of 0.3–0.8°. Twin mode components were considered irrational where angular deviation to the best-fit low-index form was $> 0.7^\circ$ (typically $> 1.5^\circ$). These results were used to classify twin modes as types 1, 2, or compound twins, as described above (Christian and Mahajan 1995). Results are summarized in Tables 4 and 5. For a given twin mode, the disorientation axis is assumed to be defined by the intersection of planes normal to η_1 for both symmetrically equivalent sets of twins. Therefore, the disorientation axis associated with $\sim \{221\} \langle 110 \rangle$ twins (Borg



◀Fig. 3 Backscattered electron images of titanite grains. Mineral abbreviations after Whitney and Evans (2009) include *Qz* quartz, *Afs* alkali feldspar, *Pl* plagioclase, *Ttn* titanite, *Zrn* zircon, *Cal* calcite, *Ap* apatite, *Mag* magnetite, *Bt* biotite, and *Hc* hercynite. **a** K-feldspar-hosted titanite in #814.85 shown in Fig. 2a. **b** Detail of the margin of the titanite grain in A, showing a fractured zircon grain and five sets of planar microstructures in alkali feldspar (black arrows). **c** Primary titanite, magnetite and apatite in a quartz domain in #1030.00 shown in Fig. 2b. **d** Apatite grains with planar fractures in an alkali feldspar domain in #1030.00. **e** Titanite in an alkali feldspar domain in #1076.16 shown in Fig. 2c. **f** Titanite with apatite, magnetite, zircon and hercynite in a quartz domain in #1076.16 shown in Fig. 2d. White arrows in **a–f** indicate the trace of transgranular fractures

1970; Borg and Heard 1972) is parallel to [102], which is coincident with the pole to (001).

Determination of slip systems

Two approaches were used to determine dislocation slip systems active in shocked titanite. The first approach involved a geometric analysis of crystal-plastic deformation bands using EBSD data, assuming a simple tilt boundary model, which has been successfully applied to low-angle boundaries in other minerals (Boyle et al. 1998; Bestmann and Prior 2003; Reddy et al. 2007). This approach assumes that disorientation axes associated with low-angle deformation bands are a consequence of geometrically necessary dislocations, and that the disorientation axis, pole to the slip plane, and Burgers vector (**b**) are orthonormal. Geometric reconstruction of low-angle tilt boundary planes must contain their traces on EBSD maps and the disorientation axis. **b** is oriented normal to the tilt boundary, and the slip plane is assumed to contain both **b** and the disorientation axis. The second approach involved automated calculation of the weighted Burgers vector (WBV) of geometrically necessary dislocations using orientation gradients in EBSD data (Wheeler et al. 2009). The WBV is defined as the net Burgers vector of dislocations that intersect an area of the EBSD map, and has been calculated by integration around the edge of a user-defined area.

In this study, an automated version of the integral approach of Wheeler et al. (2009) was implemented, whereby an EBSD map is automatically tiled into square, 20×20 -pixel ($6 \times 6 \mu\text{m}$) areas, and the WBV is calculated for each tile. This method reduces the errors on WBV in comparison to values calculated at every pixel. Results from tiles were disregarded if the square overlapped a high-angle boundary (including twin interfaces) or where the magnitude of the WBV length was below a threshold value [i.e., a minimum dislocation density, $\text{ddmin} = 0.001 (\mu\text{m})^{-1}$]. The two approaches to deducing dislocation slip systems described above are complementary: the WBV approach is automated and does not involve assumptions about low-angle boundary

geometry, whereas the low-angle boundary model also allows indexing of low-angle deformation bands.

Results

Microstructures in Chicxulub titanite

Four titanite grains were analysed, including a > 1 -mm-long grain in #814.85; a $200\text{-}\mu\text{m}$ grain in #1030.00; and two grains from #1076.16 that are $300 \mu\text{m}$ and $500 \mu\text{m}$ across, respectively (Figs. 2, 3). The titanite grains occur as inclusions within shocked and fractured alkali feldspar and quartz, and are cut by brittle fractures (Figs. 2, 3, 4, 5, 6, 7). None of the studied grains occur in discrete breccia, melt, or cataclasite veins, and are entirely enclosed within grano-toid (Fig. 2). Surrounding quartz grains contain multiple sets of PDFs, PFs, FFs (Fig. 2), and high densities of lobate/irregular Dauphiné twins (Figs. 6, 7). Calcite and TiO_2 are commonly present along fractures in titanite and along grain boundaries (Figs. 3, 4, 5, 6, 7).

All titanite grains were indexed as $\text{P}2_1/a$, with no evidence of the $\text{A}2/a$ structure. All four titanite grains contain two or more sets of polysynthetic twin lamellae (Figs. 4, 5, 6, 7). Twin lamellae are typically a few micrometres wide, straight to slightly kinked, and tapered. Others terminate against grain boundaries, fractures, or other twins, and are unevenly developed across the grains (Figs. 4, 5, 6, 7). In some grains, conspicuous sub-planar partings are present along twin interfaces (e.g., Figs. 4, 5). Each titanite grain contains two sets of twins that are disorientated from the host grain by $\sim 74^\circ/[102]$ (labelled T1 and T2 in Figs. 4, 5, 6, 7). The grain from sample #1030.00 contains a third set of twins with a disorientation relative to the host of $\sim 51^\circ/[001]$ (labelled T3 in Fig. 7a).

All host domains in the titanite grains record variable degrees of intragrain misorientation, up to $\sim 30^\circ$, which manifests as dispersion in pole figures (Figs. 4, 5, 6, 7). While some dispersion is attributed to rigid rotation of fractured blocks, a component is linked to progressive distortion and broad deformation bands with indistinct boundaries, which are the result of crystal plasticity (e.g., Fig. 5). Significant thickening of twins along deformation bands in titanite grain 1 in #1076.16 indicates that the formation of these microstructures was coeval (Fig. 8). The high angle of the twin planes to the polished surface for this sample (Fig. 8b) means that the true thickness is observed, and the twin thickness is not merely an apparent thickness, due to the plane of observation. The best-developed (strongest and most planar) deformation bands in the analysed titanite grains are defined by systematic crystallographic disorientation about an axis

Table 1 Details of samples used in this study

IODP sample ID	Depth (mbsf)	Brief thin section description
364-77-A-121-R-1-75-77	814.85	Shocked granitoid with thick cataclasite bands. Intact domains are dominated by plagioclase and alkali feldspar with perthite lamellae and local PDFs. Subordinate patches of quartz have abundant PFs and PDFs. Minor chlorite after biotite, and euhedral titanite. Accessory apatite, zircon and magnetite. Cataclasite contains patchy calcite cement
364-77-A-204-R-1-7-9 (duplicate)	1030.00	Shocked granitoid dominated by large plagioclase laths and alkali feldspar with perthite lamellae, subordinate quartz patches with abundant PFs and PDFs. Minor biotite (partially altered to chlorite) and euhedral titanite. Accessory apatite, magnetite, and zircon. Conspicuous set of transgranular planar fractures are lined with calcite
364-77-A-219-R-1-22-24	1076.16	Shocked granitoid with roughly equal proportions of plagioclase, alkali feldspar and quartz. Quartz contains abundant PFs and PDFs. Minor biotite (heterogeneously altered to chlorite), euhedral titanite and apatite. Accessory magnetite, zircon, and hercynite. Alkali feldspar contains perthite lamellae. Patchy calcite lines fractures

Sample IDs comprise information relating to the IODP catalogue system, and have the following naming convention: Expedition–Site–Hole–Core–Section–TopDepth–BottomDepth. Depths are driller depths given as metres below sea floor (mbsf)

Table 2 Scanning electron microscopy settings and electron backscatter diffraction analysis acquisition and processing parameters

SEM			
Make/model			Tescan Mira3 FEG-SEM
EBSD acquisition system			Oxford Instruments AZtec/Nordlys EBSD Detector
EDX acquisition system			Oxford Instruments AZtec/XMax 20 mm SDD
EBSD processing software			Oxford Instruments Channel 5.10
Acceleration voltage (kV)			20
Working distance (mm)			18.5
Tilt			70°
EBSD match units			
Phase	Space group	β (°)	
Titanite	15	113.93	American Mineralogist phase database (database family 725, best in family)
Quartz	152	n/a	‘Quartznew’, HKL database (Sands 1969)
Orthoclase	12	116.07	American Mineralogist phase database (Prince et al. 1973)
Bytownite	2	115.87	ICSD phase database (Facchinelli et al. 1979)
Magnetite	227	n/a	HKL phase database (Wechsler et al. 1984)
Calcite	0	n/a	HKL phase database (calcite.cry)
Zircon	141	n/a	Zircon5260, 1 atm (Hazen and Finger 1979)
Reidite	88	n/a	Reidite6032 0.69 GPa (Farnan et al. 2003)
Apatite	176	n/a	ICSD phase database
EBSP acquisition, indexing and processing			
EBSP Acquisition Speed (Hz)	40	Band detection (min/max)	6/8
EBSP Background (frames)	64	Mean angular deviation (all phases)	<1°
EBSP Binning	4 × 4	Wildspike correction	Yes
EBSP Gain	High	Nearest neighbor zero solution extrapolation	8
Hough resolution	60		

Table 3 Unit cell parameters for titanite

A (Å)	6.554
B (Å)	8.708
C (Å)	7.069
α (°)	90
β (°)	113.93
γ (°)	90

sub-parallel with the pole to $\{111\}$ (Fig. 8a, b). The map traces of the deformation bands are geometrically consistent with low-angle tilt boundaries along $\{130\}$ that contain the disorientation axis (Fig. 8b). This geometric configuration can be explained by dislocation glide with Burgers vector $\mathbf{b}=[341]$. This result is supported by weighted Burgers vector analysis, which shows WBV forms dominant clusters around $[341]$ (Fig. 8c–e), which has not previously been described in titanite.

Indexing of twins in titanite

The most common twins encountered in the Chicxulub titanite grains have disorientation relative to the host of $\sim 74^\circ/[102]$, and 180° misorientation axes that align with $\langle 110 \rangle$ of the host grains, which is coincidental with η_1 of twins described by Borg (1970) (Twins 1 and 2 in Figs. 4, 5, 6, 7; Table 5). However, reconstruction of the composition plane (K_1) using the map trace of these twins is consistent within a few degrees of $\{\bar{1}11\}$, rather than $\{221\}$ expected for Borg (1970) twins. Therefore, they define two symmetric equivalents of a previously undescribed type 2 twin mode with $K_1=\text{irrational } \sim\{\bar{1}11\}$, $\eta_1=\text{rational } \langle 110 \rangle$, and shear

plane ($S=\{112\}$) (Fig. 10, Table 5). A geometric consequence of this host–twin orientation relationship is that it results in coincidence of many crystallographic planes between twin and host that lie normal to $\eta_1 \langle 110 \rangle$, the 180° misorientation axis (Figs. 4, 5, 6, 7, Table 5).

Twins with $\sim 51^\circ/[001]$ disorientation were found in one grain (labelled T3 in Fig. 7a). The 180° misorientation axis for these twins aligns with the pole to $\{130\}$, which defines a previously undescribed twin mode $K_1=\{130\}$, $\eta_1=\text{irrational } \sim\langle 522 \rangle$, and $S=\{103\}$ (Table 5; Figs. 7b, 10). Two symmetrically equivalent variants are possible for this twin mode, which are classified as type 1 twins because they have a rational K_1 (Christian and Mahajan 1995) (Fig. 10).

Distinguishing between the newly described type 2 $\sim\{\bar{1}11\}$ twins and the established $\sim\{221\}$ twins requires care, because they have identical η_1 (parallel to $\langle 110 \rangle$) and thus produce identical disorientation axis/angle relationships using EBSD data (Fig. 10, Table 5). Therefore, correct indexing requires consideration of the trace of twin planes on the EBSD map and η_1 to reconstruct K_1 (e.g., Figs. 4, 5, 6, 7). Indexing of the newly described type 1 $\{130\} \sim\langle 522 \rangle$ twins is straightforward because it can be inferred from the disorientation angle/axis alone, as no other twins are known to have similar relationships.

Microstructures in co-existing zircon

A total of eight zircon grains were analysed in the same thin sections as the titanite grains, including zircon grains that occur as inclusions within the larger shocked titanite grains (Fig. 3a). The zircon grains are typically $<60 \mu\text{m}$

Table 4 Host–twin disorientation and misorientation calculations for titanite

Grain and twin ID	Disorientation		180° misorientation				
	Angle (°)	Axis $\langle hkl \rangle$	Angle (°)	Best-fit plane normal		Best-fit direction	
				Plane $\{hkl\}$	Deviation (°)	Axis $\{hkl\}$	Deviation (°)
121 T1	75.23	102	179.92	$\bar{1}\bar{1}0$	0.66	$24\bar{1}$	4.53
121 T2	72.27	$\bar{1}0\bar{2}$	179.33	$1\bar{1}0$	1.59	$2\bar{4}\bar{1}$	2.60
121 T(i)	73.32	102	179.34	$\bar{1}\bar{1}0$	0.67	$24\bar{1}$	4.01
204 T1	74.16	102	179.98	110	0.23	$24\bar{1}$	4.12
204 T2	74.02	102	179.65	$\bar{1}\bar{1}0$	0.22	$24\bar{1}$	4.07
204 T3	51.30	001	179.97	$\bar{3}\bar{4}\bar{1}$	2.11	$\bar{1}\bar{3}0$	0.20
219_1 T1	73.93	$\bar{1}0\bar{2}$	179.93	$\bar{1}10$	0.08	$24\bar{1}$	3.88
219_1 T2	74.17	$\bar{1}0\bar{2}$	176.85	$\bar{1}10$	0.73	$2\bar{4}\bar{1}$	4.37
219_2 T1	72.12	102	178.20	110	1.06	$24\bar{1}$	3.53
219_2 T2	72.58	102	179.98	$\bar{1}\bar{1}0$	0.75	$24\bar{1}$	3.18
Borg (1970)	~ 73	102	180	110	n/a	221	n/a

Table 5 Twinning in titanite

Source reference	Borg (1970)	Borg (1970)	This study	This study
Examples			#814.85 (T1, T2), #1030.00 (T1, T2), #1076.16_1 (T1, T2), #1076.16_2 (T1, T2)	#1030.00 (T3)
Twin mode				
K_1 (slip plane, plane of no distortion, composition plane)	Irrational ~{221}	{ $\bar{1}31$ }	Irrational ~{ $\bar{1}11$ }	{130}
η_1 (slip direction)	<110>	Irrational	<110>	Irrational ~<522>
K_2 (conjugate plane of no distortion)	{ $\bar{1}31$ }	Irrational ~{221}	Rational ???	???
η_2 (axis of principal zone)	Irrational	<110>	???	???
S (plane of deformation)	Irrational ~{ $\bar{1}\bar{1}2$ }		{112}	(10 $\bar{3}$)
Twin type	2	1	2	1
Disorientation				
Angle	~ 74°	~ 74°	~ 74°	~ 53°
Axis	<102>	<102>	<102>	[003]
Coincident planes				
(001)			Yes	No
{111}			Yes	No
{ $\bar{1}11$ }			Yes	No
{112}			Yes	No
{ $\bar{1}12$ }			Yes	No
{221}			Yes	No
{22 $\bar{1}$ }			Yes	No
{24 $\bar{1}$ }			(Yes?)	No
{130}			No	Yes
{ $\bar{1}03$ }			No	Yes
Coincident directions				
[001]			No	Yes
<110>			Yes	No
< $\bar{1}10$ >			Yes	No
<34 $\bar{1}$ >			No	No

Disorientation = angle/axis that describes the minimum misorientation between the twin and the host. ‘Coincidence’ is defined as <0.7° angular deviation

across, euhedral to anhedral in shape, with some grains preserving evidence of growth zoning. All of the grains are fractured, and most of the observed variations in crystallographic orientation, shown by variations in colour in EBSD orientation maps and pole figures in Fig. 9, are related to rotation of rigid blocks separated by fractures (Fig. 9a, b, d, f, g). However, the zircon grains preserve minor evidence (<5°) of crystal-plastic strain, seen as smooth, systematic gradients in orientation that are not related to fractures (Fig. 9a, e, h). No microstructures diagnostic of shock metamorphism, such as {112} twins, the high-pressure polymorph reidite, granular neoblasts, or dissociation textures (e.g. Timms et al. 2017b), were

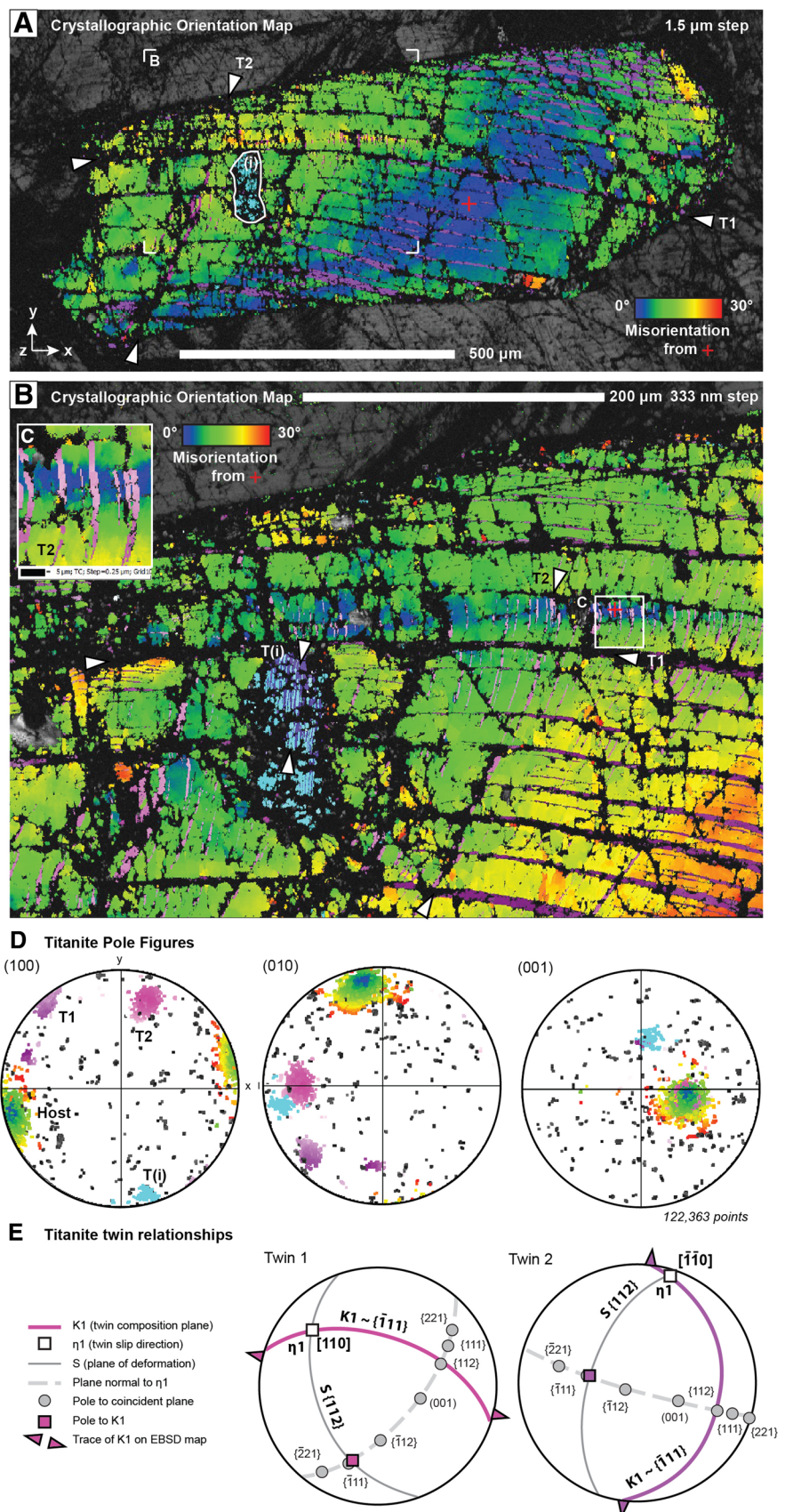
detected in the zircon grains analysed. If present, these microstructures would have been readily detected by the EBSD analysis utilized in this study.

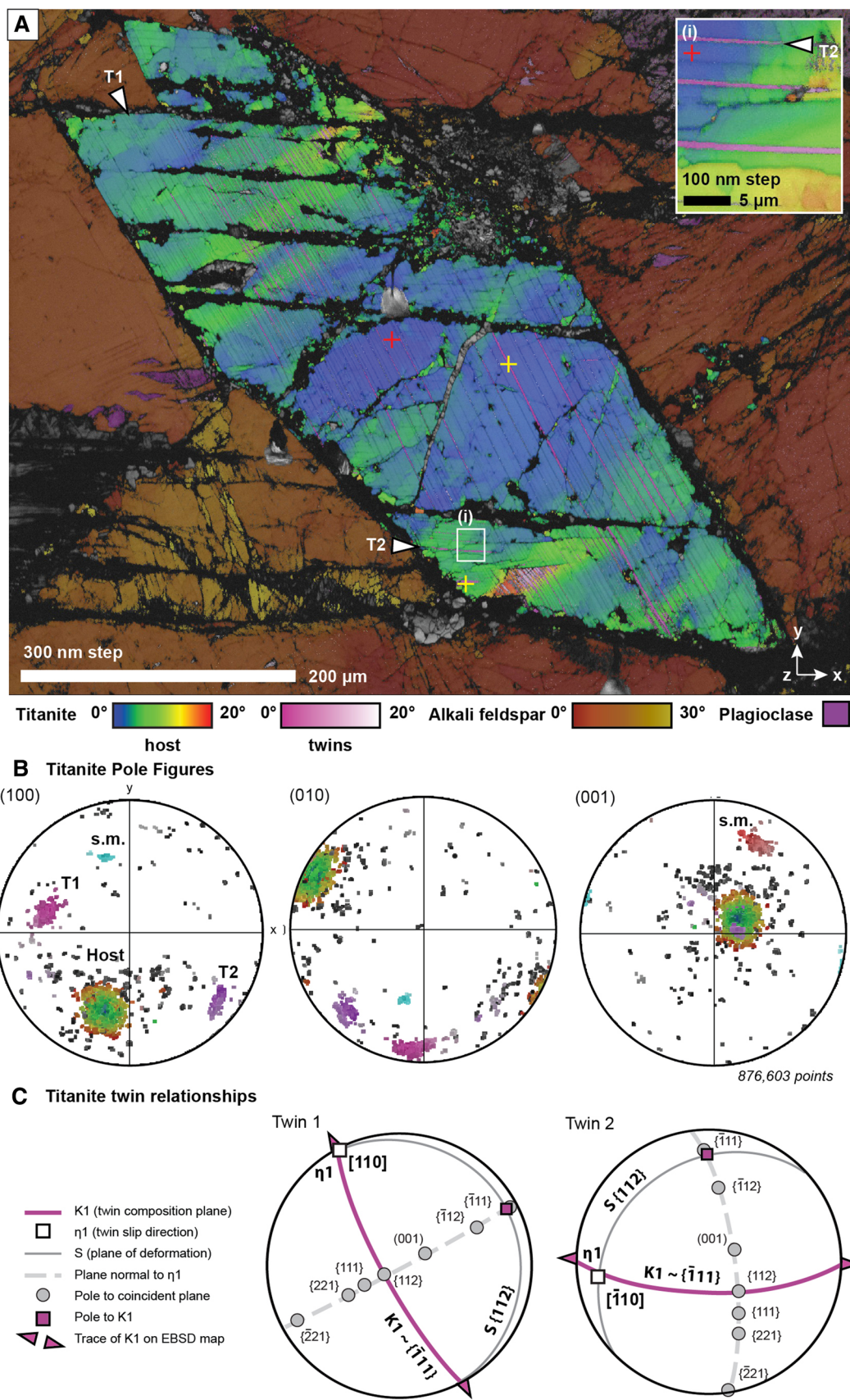
Discussion

New titanite twins in Chicxulub shocked granite

The two twin types found in Chicxulub titanite described here have not been reported previously in tectonically deformed titanite, and we propose that they are a product of shock metamorphism during hypervelocity-impact

Fig. 4 Microstructure of titanite grain from #814.85 (Fig. 3a). **a** Cumulative disorientation map showing 30° variation across the grain and two sets of twins (labelled T1 and T2). An inclusion of a titanite grain with a different orientation is shown by white outline labelled (i). **b, c** Detailed maps of region shown in **a**. **d** Pole figures for (100), (010) and (001). Lower hemisphere, equal area projections in the sample x - y - z reference frame. **e** Crystallographic relationships between twin and host for twins shown in (a-c) in the sample reference frame





◀Fig. 5 Microstructure of titanite grain 1 from #1076.16 (Fig. 3e). **a** Cumulative disorientation map showing 20° variation across the titanite grain and two sets of twins (labelled T1 and T2). Fractures and perthitic lamellae are present in surrounding K-feldspar grains. Inset (i) is a detailed map showing T2 twins. **b** Pole figures for (100), (010) and (001). Sparse systematically misindexed points at host-twin interfaces (labelled as ‘sm’) have disorientation relationships of 98°/⟨2̄12⟩ and 180°/[003]. Lower hemisphere, equal area projections in the sample $x-y-z$ reference frame. **c** Crystallographic relationships between twin and host for twins shown in **a** in the sample reference frame

conditions given the occurrence in granitoid with well-documented quartz microstructures indicative of shock pressures of about 12–17 GPa. Thus, our results offer new insights into how titanite deforms in impact environments. The new twin modes are geometrically distinct from previously established mechanical and/or growth twins in titanite (e.g. Borg 1970) (Fig. 10; Tables 4, 5). The most common twins in Chicxulub titanite grains have irrational composition planes (K_1) that are within a few degrees of {1̄11}, and a rational $\eta_1 = <110>$, and $(S) = \{112\}$. Chicxulub titanite grains typically have two sets of $\sim\{1̄11\}<110>$ twins, which is the maximum number possible given the monoclinic symmetry. One unusual aspect of $\sim\{1̄11\}<110>$ twins is that they share an identical twin–host minimum misorientation (disorientation) relationship with previously established $\sim\{221\}<110>$ twins (e.g., Borg, 1970), and thus the two twin types cannot be distinguished solely based on disorientation angle/axis measurements provided by EBSD analysis. Identification of each twin type thus requires indexing of the composition planes (twin planes), which we calculated using a MATLAB script.

A set of lamellar twins with a different host–twin disorientation crystallographic relationship of $\sim 51^\circ/[001]$ was found in one Chicxulub grain (labelled T3 in Fig. 2a). These twins represent a second previously undescribed twin mode in titanite, whereby $K_1 = \{130\}$, $\eta_1 = \text{irrational } \sim <522>$, and $S = (10\bar{3})$ (Table 4; Figs. 7b, 9c). Indexing of the newly described $\{130\} \sim <522>$ twins is straightforward because it can be inferred from the disorientation angle/axis relations provided by EBSD data.

Concurrent deformation processes in titanite during shock metamorphism

The thickening of $\sim\{1̄11\}<110>$ mechanical twins along {130} deformation bands clearly indicates that dislocations with \mathbf{b} [341] occurred concurrently with twinning (Fig. 8). Concurrent crystal plasticity could potentially have affected twinning in two different ways: (1) the widening of twins was mechanically facilitated by $\{112\}$ [341] dislocation activity,

and/or (2) the formation of deformation bands locally re-orientated titanite into a more favourable orientation for twinning with respect to the stress field of the shock wave. Given that the slip vector for twinning and Burgers vector for dislocation glide are similarly oriented (i.e., twinning $\eta_1 = <110>$ and dislocation $\mathbf{b} = <341>$, respectively, are within $\sim 10^\circ$ of one another), it is possible that these two types of microstructure have accommodated shock deformation in a coherent and systematic way similar to cross slip. However, the effects of localized re-orientation in deformation bands on the ease of twinning cannot be resolved without additional information about the nature of the stress–strain field associated with the passing shock wave relative to the orientation of the grains and critically resolved shear stress for twinning. Nevertheless, the absence of {130} deformation bands in other shock-twinned grains in this study indicates that concurrent [341] dislocation slip is not a requirement for these twin modes in titanite.

Petrological implications of the new twin modes in titanite

Titanite in the target rocks that formed the peak ring at the Chicxulub crater responded to the ~ 12 –17 GPa bulk peak shock pressure principally by $\sim\{1̄11\}<110>$ twinning, with minor {130} $\sim <522>$ twinning and coeval crystal plasticity. Zircon, a tetragonal accessory phase, is also known to form deformation twins and other microstructures during shock deformation (Fig. 11). In contrast to titanite, zircon grains in the same samples do not record diagnostic shock-/impact-related microstructures (Fig. 9), which is consistent with them having experienced shock pressure < 20 GPa (e.g. Timms et al. 2017b). In this respect, titanite appears similar to xenotime, which has also been shown by empirical calibration with quartz and zircon to form impact-related deformation twins and plastic deformation at shock pressures < 20 GPa (Cavosie et al. 2016b) (Fig. 11). Differences in the response of titanite and other accessory minerals to shock deformation are shown in Fig. 11. The variable microstructural responses are presumably related to the intrinsic material properties of the different minerals, such as elasticity and yield strength for various failure modes, which are largely controlled by crystal structure. Phase transformations and reactions that determine phase stability through shock conditions are also important.

The precise details of the kinetics, nucleation stress, and critically resolved shear stress for the newly described twin modes are yet to be determined by theoretical or experimental means. However, unlike for shock twinning and dislocations in zircon (Timms et al. 2018), theoretical calculations are inhibited by the current lack of published elastic constants for $P2_1/a$ titanite. More rigorous investigations into the

Fig. 6 Microstructure of titanite grain 2 from #1076.16 (Fig. 3f). **a** Cumulative disorientation map showing 30° variation across the titanite grain and two sets of twins (labelled T1 and T2). Dauphiné twins are present in surrounding quartz grains, and magnetite contains thin lamellar twins. Inset (i) is a detailed map showing T2 twins. **b** Pole figures for (100), (010) and (001). Lower hemisphere, equal area projections in the sample x–y–z reference frame. **c** Crystallographic relationships between twin and host for twins shown in **a** in the sample reference frame

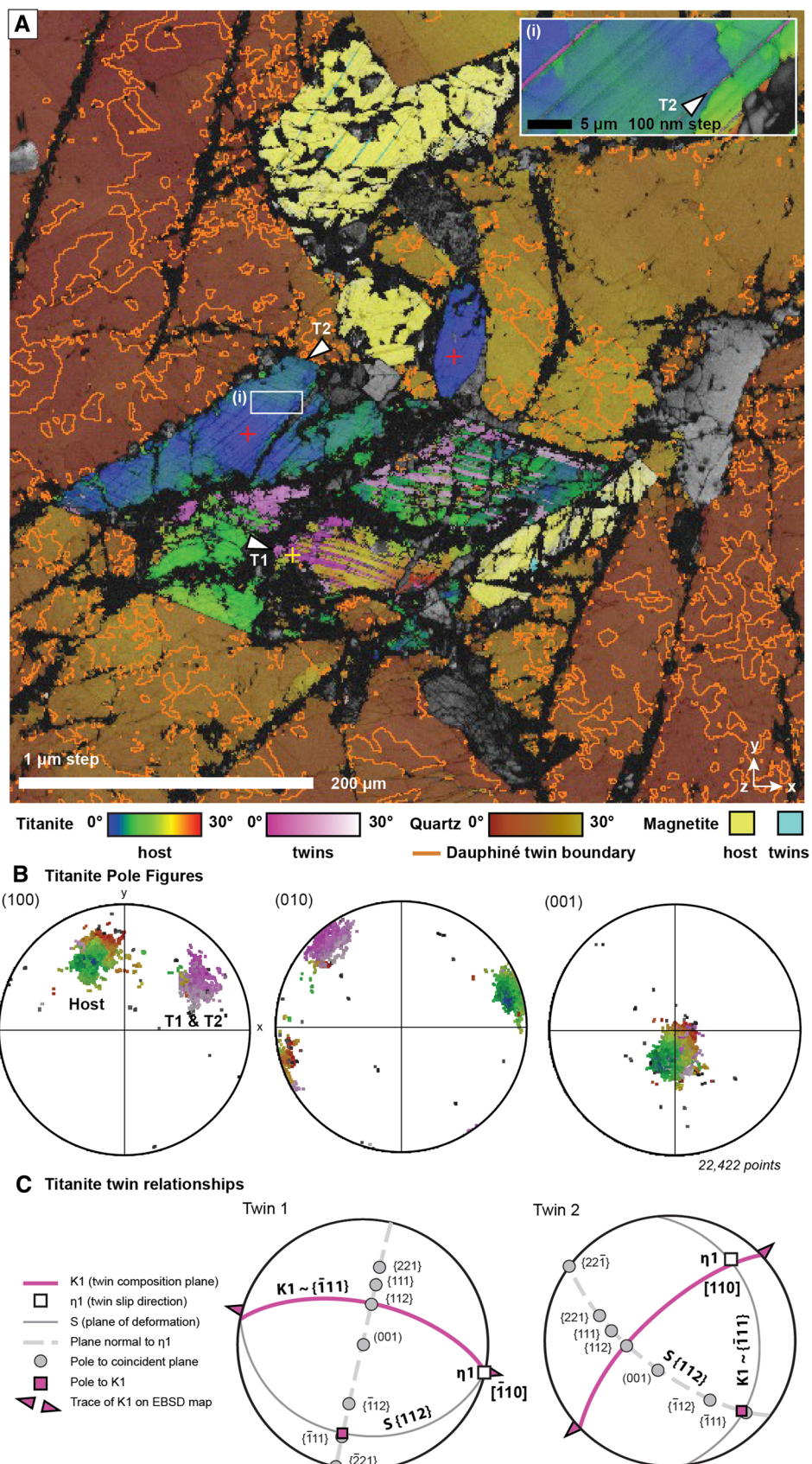
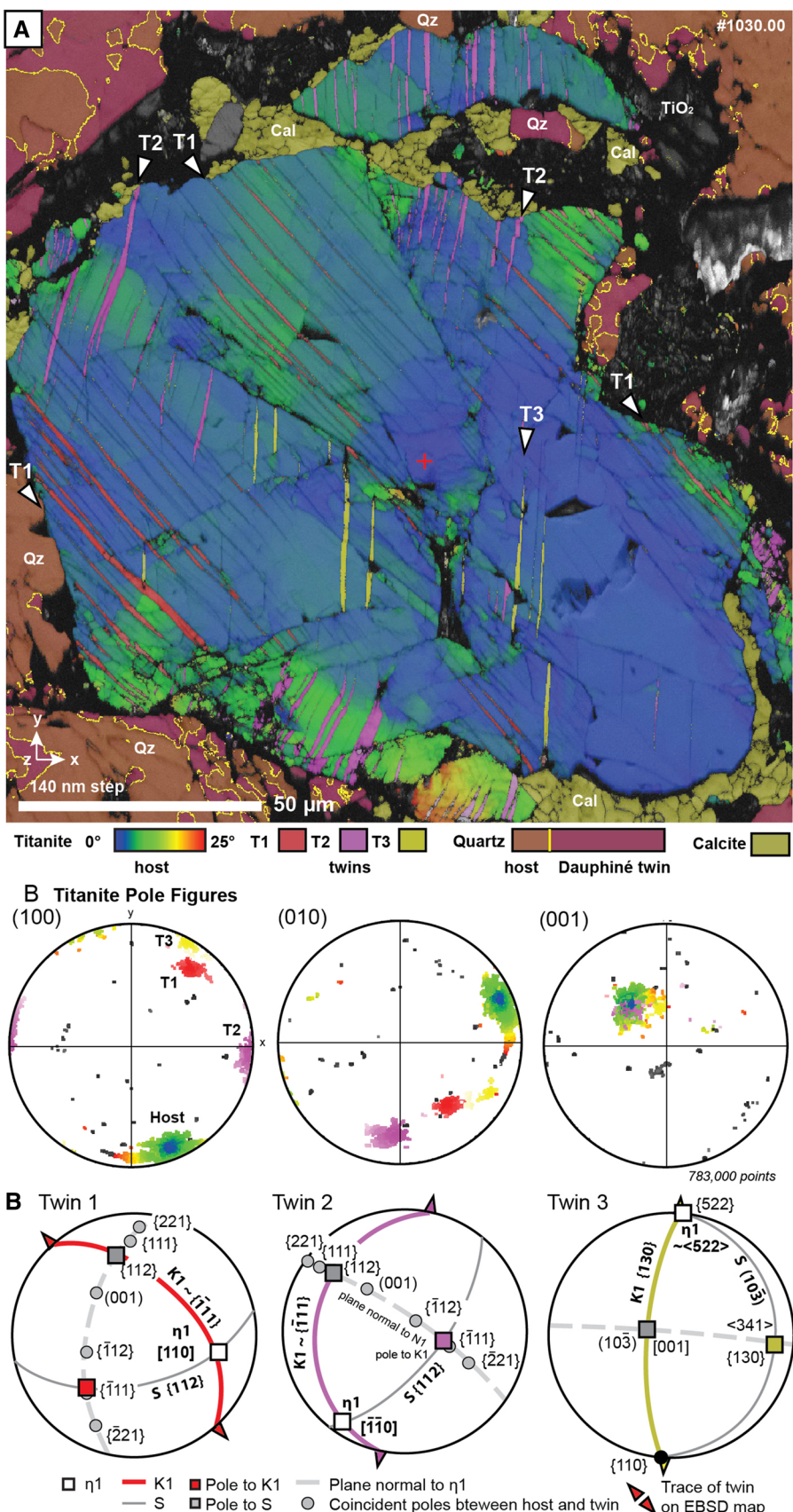


Fig. 7 **a** EBSD map of titanite in sample #1030.00 from the Chicxulub crater peak ring (Fig. 3c). Titanite is coloured for cumulative disorientation relative to reference orientation (red cross) and has three sets of twins (T1, T2, and T3). It is surrounded by quartz with Dauphiné twins (Qz, orange/red), calcite (Cal, yellow) and TiO_2 . Inset (i) shows pole figure for (100) in sample reference frame. **b** Crystallographic relationships between twins T1, T2, and T3 and host grain. Several low-index poles to coincident planes (grey circles) align along the plane normal to η_1 for Twins 1 and 2. Lower hemisphere, equal area projections in the sample x - y - z reference frame



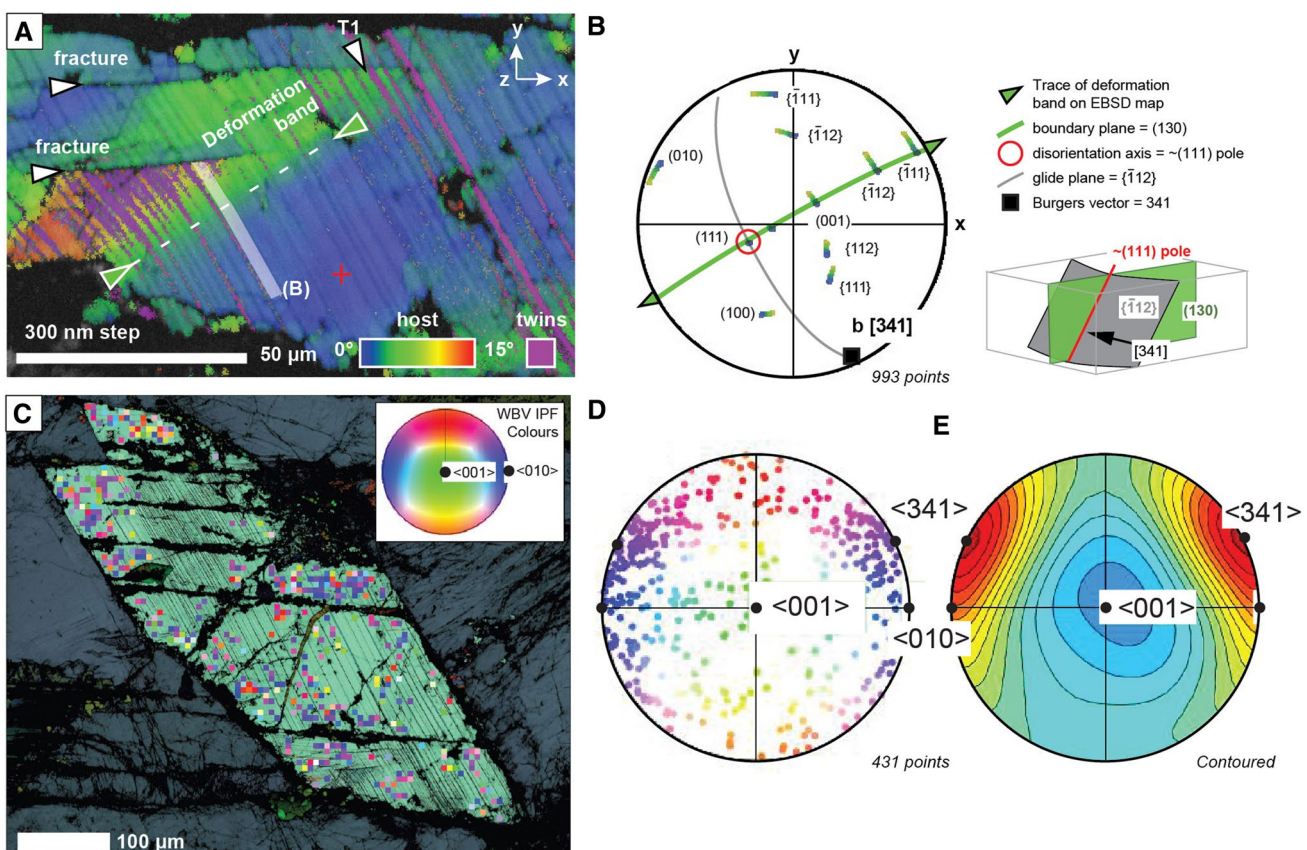


Fig. 8 **a** Detailed EBSD map of grain 1 from #1076.16 shown in Fig. 5. Titanite is coloured for cumulative disorientation relative to reference orientation (red cross) and twins (purple, labelled T1). Crystal-plastic deformation band (green–orange domain) has a well-defined lower boundary trace (white dashed line), and is displaced by brittle fractures. Twin lamellae are thicker within the deformation band. **b** Composite pole figure of data shown by the white box in **a**, plotted in the sample x – y – z reference frame. Crystallographic data show a systematic dispersion about a disorientation axis approximately parallel to the pole to (111). The deformation band is consistent with a (130) tilt boundary geometry that contains the disorientation axis and the trend of the deformation band on the polished surface. The dominant dislocation slip system that contributed to the deformation bands involved glide with a [341] Burgers vector. **c** EBSD map of the entire grain showing results of automated weighted Burgers vector (WBV) analysis. Superimposed squares indicate $6 \times 6 \mu\text{m}$ tiles from which the integral WBV was calculated. Tiles that overlap with twin domains have been disregarded. Tiles are coloured for WBV orientation using an inverted pole figure (IPF) colour scheme. **d** Pole figure of WBV data shown in **c**, plotted in crystallographic reference frame. **e** Contoured pole figure of data shown in **d**, indicating dominance of WBV parallel to [341]

entation axis and the trend of the deformation band on the polished surface. The dominant dislocation slip system that contributed to the deformation bands involved glide with a [341] Burgers vector. **c** EBSD map of the entire grain showing results of automated weighted Burgers vector (WBV) analysis. Superimposed squares indicate $6 \times 6 \mu\text{m}$ tiles from which the integral WBV was calculated. Tiles that overlap with twin domains have been disregarded. Tiles are coloured for WBV orientation using an inverted pole figure (IPF) colour scheme. **d** Pole figure of WBV data shown in **c**, plotted in crystallographic reference frame. **e** Contoured pole figure of data shown in **d**, indicating dominance of WBV parallel to [341]

shock response of titanite via laboratory shock deformation experiments remain an avenue for future research. Furthermore, very few quantitative microstructural studies of naturally deformed titanite from tectonic and/or impact environments are currently available (Papapavlou et al. 2017, 2018). Thus, further studies of naturally shocked and tectonically deformed titanite are required to provide better constraints on formation conditions for different twin modes.

The discovery of new titanite twin modes in shocked target rocks at Chicxulub represents the first steps toward developing a twin-based framework for using titanite to distinguish tectonic versus impact-related deformation, similar to the approach developed recently for monazite (Erickson et al. 2016). Titanite appears to behave similar to

monazite in that a range of twin modes have been reported, with empirical studies indicating that certain twin types uniquely form as a consequence of shock deformation. Cleavage along $\sim \{111\}$ twin planes shown by several of the Chicxulub grains is different to the dominant cleavage orientations reported for titanite from the Ries crater (Abadian 1972). If titanite commonly cleaves along twin lamellae, then observations of cleavage made by Abadian (1972) may be an indication that additional shock twin modes could be revealed via detailed studies of shocked titanite from other impact structures (Papapavlou et al. 2018). Our findings further indicate that additional information is required to singular twin disorientation axes produced from EBSD data to correctly index twins in titanite.

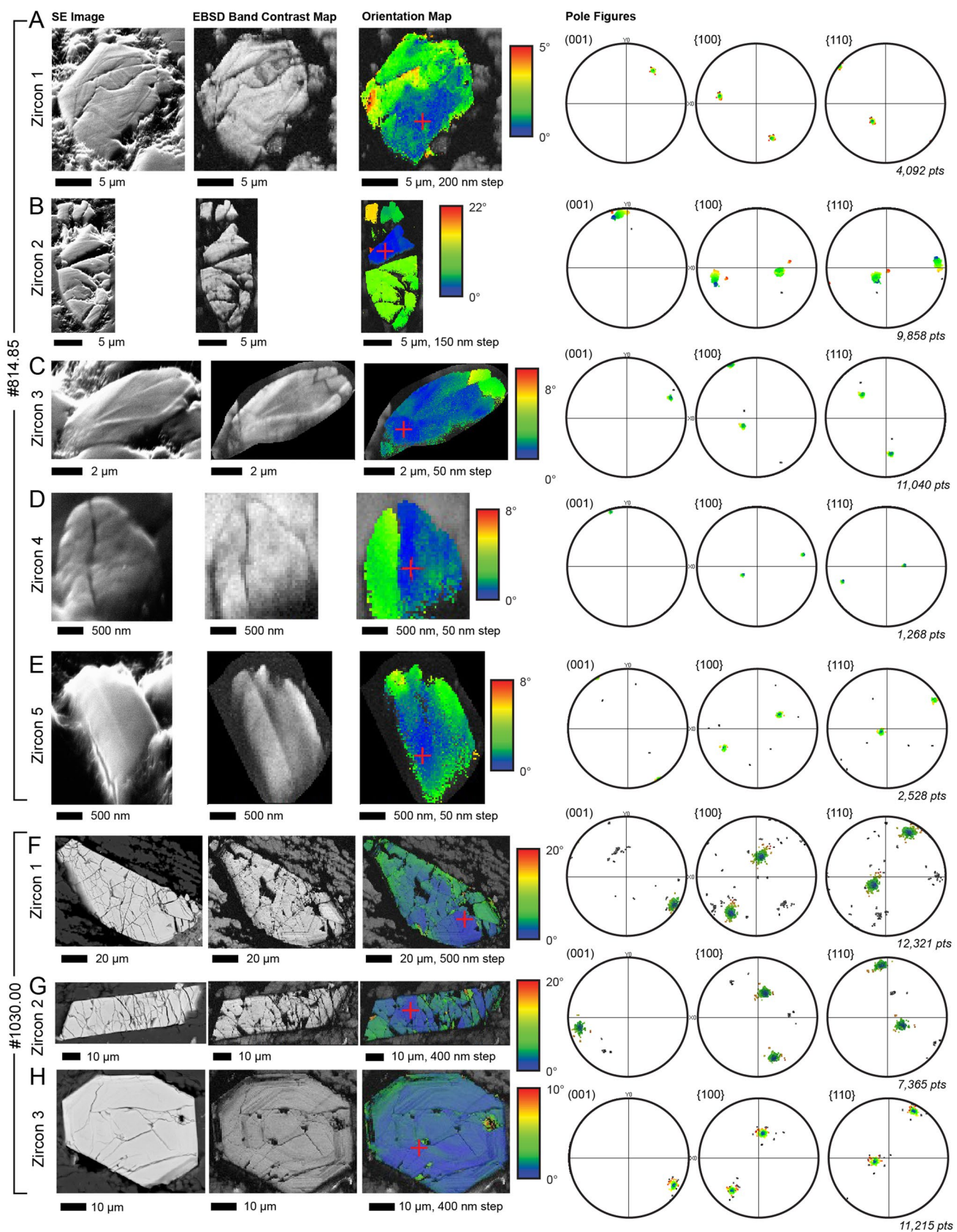


Fig. 9 Microstructure of zircon grains associated with titanite from samples #814.85 and #1030.00 of this study

Fig. 10 Summary of the geometric elements of deformation microstructures in titanite. Pole figures **a** $\sim\{221\}<110>$ twins after Borg (1970). **b** $\sim\{111\}<110>$ twins, this study. **c** $\{130\}\sim<522>$ twins, this study. **d** $\{130\}$ deformation bands, this study. The two possible symmetric equivalent variants are shown for each type of microstructure. Microstructures shown in **b–d** have not been described from tectonically deformed titanite

Broader applications of deformation twin systematics

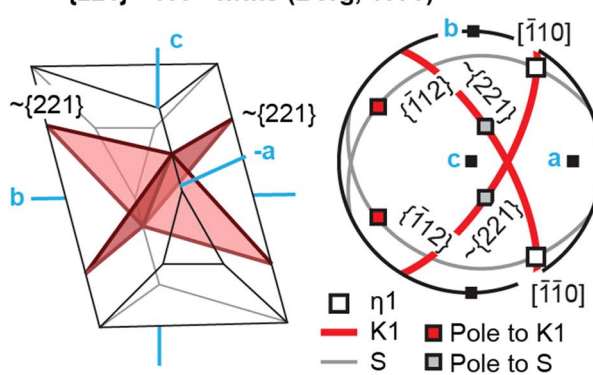
In this study, we outline an approach for rigorous indexing and classification of deformation twins from EBSD data based on geometric considerations of Christian and Mahajan (1995). We demonstrate the importance of our approach for distinguishing twin modes in titanite formed in tectonic versus shock settings. This approach builds on the method outlined by Erickson et al. (2016) that led to the discovery of new twin modes in monazite, and can be applied to other minerals that form twins, such as ilmenite, rutile, and pyrrhotite, which could be useful for better understanding deformation of rocks in both tectonic and impact settings.

Conclusions

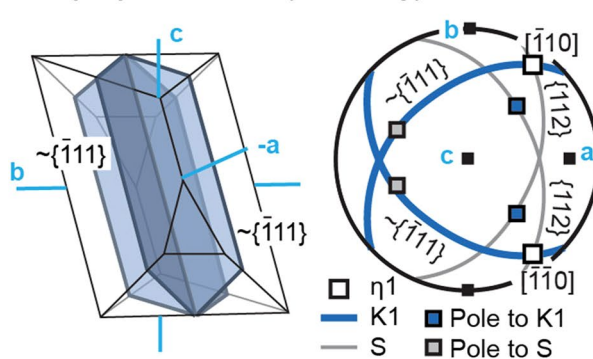
Titanite is a common accessory phase in a variety of rock types (Frost et al. 2001), which has the propensity to record impact-related microstructures. Specifically, we demonstrate titanite undergoes shock-related deformation twinning along $\sim\{111\}$ and $\{130\}$, as recorded in the shocked target rocks of the Chicxulub impact structure over the pressure range between 12 ± 5 and $\sim 17 \pm 5$ GPa. These twin modes can form concurrently with deformation bands along $\{130\}$ resulting from dislocation migration with a $<341>$ Burgers vector. The newly described twin modes in $\sim\{111\}$ and $\{130\}$ are different from previously reported $\sim\{221\}$ twins from tectonically deformed titanite, and we, therefore, hypothesize that they are indicative of shock conditions. We have defined geometric criteria for distinguishing these various twins in titanite, which highlights the importance of utilizing a rigorous approach for indexing twins. Furthermore, as this accessory mineral may be susceptible to age-resetting during deformation (Papapavlou et al. 2017, 2018), we propose that our findings greatly increase the potential of titanite as a diagnostic recorder of impact events in the geological record.

Acknowledgements The Chicxulub drilling expedition was funded by the IODP as Expedition 364 with co-funding from the ICDP, implementation by ECORD, and contributions and logistical support from the Yucatán state government and UNAM. This research used samples provided by the IODP, funding provided by a UK IODP NERC Grant (NE/P011195/1), and a Tescan Mira3 FE-SEM (ARC LE130100053)

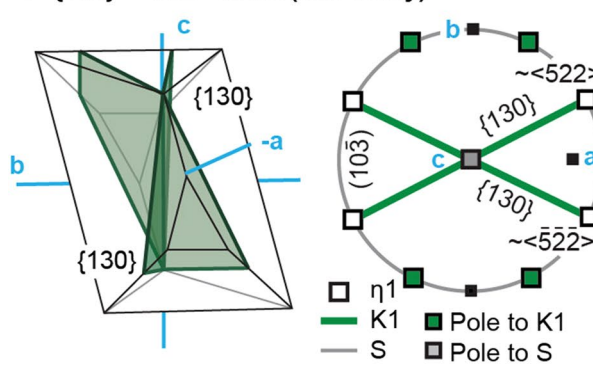
A $\sim\{221\}<110>$ twins (Borg, 1970)



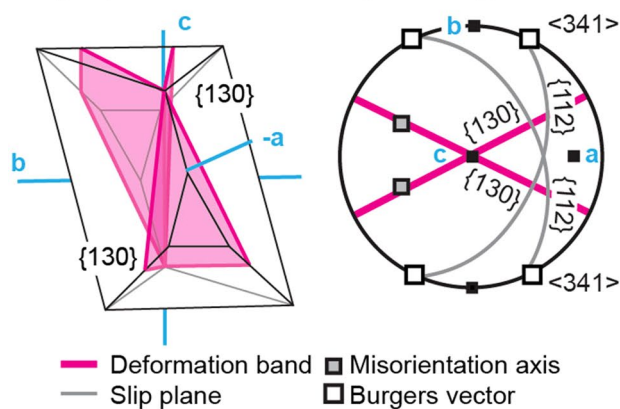
B $\sim\{111\}<110>$ twins (this study)



C $\{130\}\sim<522>$ twins (this study)



D $\{130\}$ deformation bands (this study)



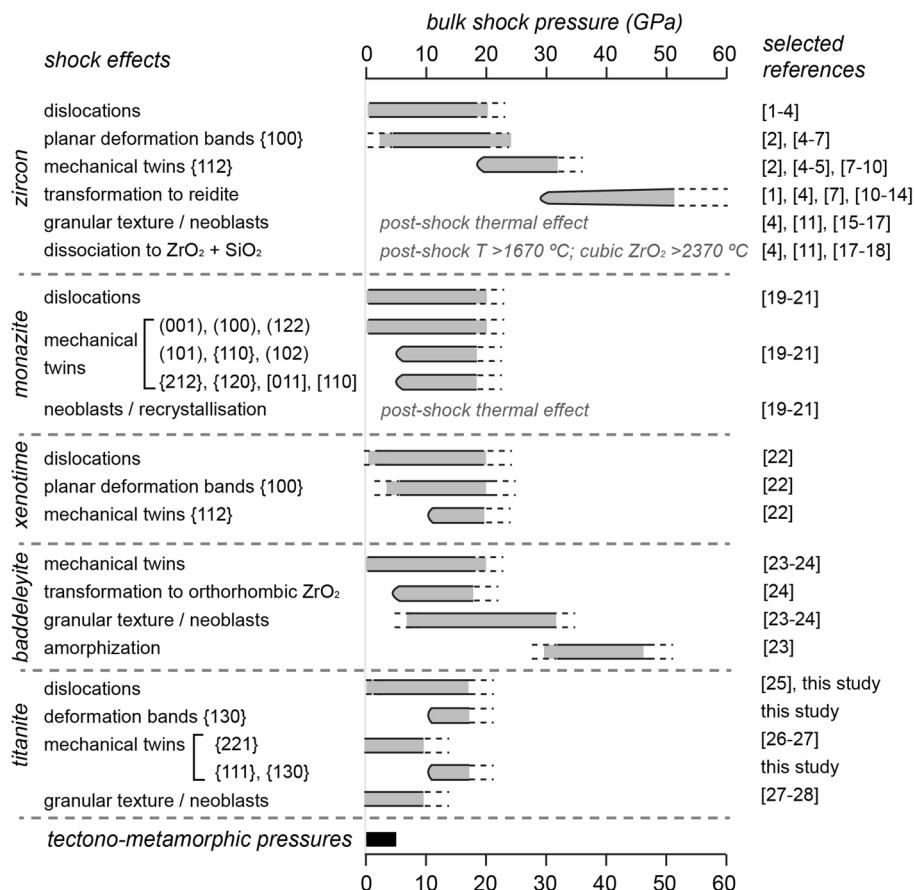


Fig. 11 Accessory phases as indicators of shock metamorphism. [1]—Leroux et al. (1999), [2]—Timms et al. (2012), [3]—Moser et al. (2009), [4]—Timms et al. (2017a), [5]—Erickson et al. (2013), [6]—Nemchin et al. (2009), [7]—Timms et al. (2018), [8]—Moser et al. (2011), [9]—Thomson et al. (2014), [10]—Cox et al. (2018), [11]—Wittmann et al. (2006), [12]—Cavosie et al. (2015b), [13]—Reddy et al. (2015), [14]—Erickson et al. (2017a), [15]—Cavosie et al. (2015a), [16]—Cavosie et al. (2016a), [17]—Cavosie et al. (2018b), [18]—Timms et al. (2017b), [19]—Erickson et al. (2015),

[20]—Erickson et al. (2016), [21]—Erickson et al. (2017b), [22]—Cavosie et al. (2016b), [23]—Darling et al. (2016), [24]—White et al. (2018), [25]—Müller and Franz (2004), [26]—Borg (1970), [27]—Papapavlou et al. (2018), [28]—Papapavlou et al. (2017). Note that the pressures indicated are specifically mean (bulk) pressures for rocks with negligible initial porosity, such as the granitoids in this study. The effects of porosity on bulk shock pressure have been treated elsewhere (e.g., Gündemeister et al. 2013)

at the John de Laeter Centre, Curtin University. ASPR received support from the Barringer Family Fund for Meteorite Impact Research and STFC (ST/J001260/1), and thanks R.A.F. Grieve and G.R. Osinski for their support. AJC acknowledges support from the NASA Astrobiology program (Grant #NNA13AA94A) and a Curtin Senior Research Fellowship. TME acknowledges support from a Lunar and Planetary Institute Postdoctoral Research Fellowship, the Center for Lunar Science and Exploration, and D. Kring. AW, SG, and CR are supported by National Science Foundation (OCE-1737087 and 1737351). This is a UTIG Contribution #3447. J. Darling, W.U. Reimold, and two anonymous reviewers are thanked for their comments on earlier versions of the manuscript. We thank D. Rubatto for editorial handling.

IODP-ICDP Expedition 364 Scientists, S. P. S. Gulick: Institute for Geophysics and Department of Geological Sciences, Jackson School of Geosciences, University of Texas at Austin, Austin, TX, USA, J. V. Morgan: Department of Earth Science and Engineering, Imperial College London, London, UK, E. Chenot: Géosciences Montpellier, Université de Montpellier, Montpellier, France, G. L. Christeson: Institute for Geophysics, Jackson School of Geosciences, University of Texas

at Austin, Austin, TX, USA, P. Claeys: Analytical, Environmental and Geo-Chemistry, Vrije Universiteit Brussel, Brussels, Belgium, C. S. Cockell: Centre for Astrobiology, School of Physics and Astronomy, University of Edinburgh, Edinburgh, UK, M. J. L. Coolen: Department of Chemistry, WA-Organic and Isotope Geochemistry Centre, Curtin University, Perth, Western Australia, Australia, L. Ferrière: Natural History Museum, Vienna, Austria, C. Gebhardt: Alfred Wegener Institute Helmholtz Centre of Polar and Marine Research, Bremerhaven, Germany, K. Goto: International Research Institute of Disaster Science, Tohoku University, Sendai, Japan, S. Green: British Geological Survey, Edinburgh, UK, H. Jones: Department of Geosciences, Pennsylvania State University, University Park, PA, USA, D. A. Kring: Lunar and Planetary Institute, Houston, TX, USA, J. Lofi: Géosciences Montpellier, Université de Montpellier, Montpellier, France, C. M. Lowery: Institute for Geophysics, Jackson School of Geosciences, University of Texas at Austin, Austin, TX, USA, R. Ocampo-Torres: Groupe de Physico-Chimie de l'Atmosphère, L'Institut de Chimie et Procédés pour l'Énergie, l'Environnement et la Santé (ICPEES),

Université de Strasbourg, Strasbourg, France, L. Perez-Cruz: Instituto de Geofísica, Universidad Nacional Autónoma De México, Ciudad De México, Mexico, A. E. Pickersgill: School of Geographical and Earth Sciences, University of Glasgow, Glasgow, UK, Argon Isotope Facility, Scottish Universities Environmental Research Centre, East Kilbride, UK, M. H. Poelchau: Institut für Geo- und Umweltnaturwissenschaften, Albert-Ludwigs-Universität, Freiburg, Germany, A. S. P. Rae: Department of Earth Science and Engineering, Imperial College London, London, UK, Institut für Geo- und Umweltnaturwissenschaften, Albert-Ludwigs-Universität, Freiburg, Germany, C. Rasmussen: Institute for Geophysics, Jackson School of Geosciences, University of Texas at Austin, Austin, TX, USA, Department of Geology and Geophysics, University of Utah, Salt Lake City, UT, USA, M. Rebollo-Vieyra: Independent consultant, Cancun, Mexico, U. Riller: Institut für Geologie, Universität Hamburg, Hamburg, Germany, H. Sato: Japan Agency for Marine-Earth Science and Technology, Kanagawa, Japan, J. Smit: Faculty of Earth and Life Sciences (FALW), Vrije Universiteit Amsterdam, Amsterdam, Netherlands, S. M. Tikoo: Earth and Planetary Sciences, Rutgers University, New Brunswick, NJ, USA, N. Tomioka: Kochi Institute for Core Sample Research, Japan Agency for Marine-Earth Science and Technology, Kochi, Japan, J. Urrutia-Fucugauchi: Instituto de Geofísica, Universidad Nacional Autónoma De México, Ciudad De México, Mexico, M. T. Whalen: Department of Geosciences, University of Alaska Fairbanks, Fairbanks, AK, USA, A. Wittmann: Eyring Materials Center, Arizona State University, Tempe, AZ, USA, L. Xiao: School of Earth Sciences, Planetary Science Institute, China University of Geosciences, Wuhan, China, K. E. Yamaguchi: Department of Chemistry, Toho University, Chiba, Japan, NASA Astrobiology Institute.

References

Abadian M (1972) Petrography, shock metamorphism and genesis of polymict crystalline breccias in the Nördlinger Ries. *Contrib Miner Petrol* 35(3):245

Angel RJ, Kunz M, Miletich R, Woodland AB, Koch M, Xirouchakis D (1999) High-pressure phase transition in CaTiOSiO₄ titanite. *Phase Transit* 68(3):533–543. <https://doi.org/10.1080/0141159908224532>

Bestmann M, Prior DJ (2003) Intragranular dynamic recrystallization in naturally deformed calcite marble: diffusion accommodated grain boundary sliding as a result of subgrain rotation recrystallization. *J Struct Geol* 25(10):1597–1613. [https://doi.org/10.1016/s0191-8141\(03\)00006-3](https://doi.org/10.1016/s0191-8141(03)00006-3)

Biren MB, Spray JG (2011) Shock veins in the central uplift of the Manicouagan impact structure: context and genesis. *Earth Planet Sci Lett* 303(3–4):310–322. <https://doi.org/10.1016/j.epsl.2011.01.003>

Bonamici CE, Fanning CM, Kozdon R, Fournelle JH, Valley JW (2015) Combined oxygen-isotope and U-Pb zoning studies of titanite: new criteria for age preservation. *Chem Geol* 398:70–84. <https://doi.org/10.1016/j.chemgeo.2015.02.002>

Borg IY (1970) Mechanical <110> twinning in shocked sphene. *Am Miner* 55:1876–1888

Borg IY, Heard HC (1972) Mechanical twinning in sphene at 8 Kbar, 25° to 500° C. *Geol Soc Am Memoirs* 132:585–592

Boyle AP, Prior DJ, Banham MH, Timms NE (1998) Plastic deformation of metamorphic pyrite: new evidence from electron-backscatter diffraction and forescatter orientation-contrast imaging. *Miner Deposit* 34(1):71–81. <https://doi.org/10.1007/s001260050186>

Bunge HJ (1981) Fabric analysis by orientation distribution functions. *Tectonophysics* 78(1–4):1–21

Cavosie AJ, Erickson TM, Timms NE, Reddy SM, Talavera C, Montalvo SD, Pincus MR, Gibbon RJ, Moser D (2015a) A terrestrial perspective on using ex situ shocked zircons to date lunar impacts. *Geology* 43(11):999–1002. <https://doi.org/10.1130/g37059.1>

Cavosie AJ, Erickson TM, Timms NE (2015b) Nanoscale records of ancient shock deformation: reidite (ZrSiO₄) in sandstone at the Ordovician Rock Elm impact crater. *Geology* 43(4):315–318. <https://doi.org/10.1130/g36489.1>

Cavosie AJ, Timms NE, Erickson TM, Hagerty JJ, Hörz F (2016a) Transformations to granular zircon revealed: twinning, reidite, and ZrO₂ in shocked zircon from Meteor Crater. *Geology* 44(9):703–706

Cavosie AJ, Montalvo PE, Timms NE, Reddy SM (2016b) Nanoscale deformation twinning in xenotime, a new shocked mineral, from the Santa Fe impact structure (New Mexico, USA). *Geology* 44(10):803–806

Cavosie AJ, Timms NE, Erickson TM, Koeberl C (2018a) New clues from Earth's most elusive impact crater: evidence of reidite in Australasian tektites from Thailand. *Geology* 46(3):203–206. <https://doi.org/10.1130/g39711.1>

Cavosie AJ, Timms NE, Ferrière L, Rochette P (2018b) FRIGN zircon—the only terrestrial mineral diagnostic of high-pressure and high-temperature shock deformation. *Geology* 46(10):891–894. <https://doi.org/10.1130/G45079.1>

Chao ECT (1968) Pressure and temperature histories of impact metamorphosed rocks—based on petrographic observations. In: French BM, Short NM (eds) Shock metamorphism of natural materials. Mono Press, Baltimore, pp 135–158

Cho JH, Rollett AD, Oh KH (2005) Determination of a mean orientation in electron backscatter diffraction measurements. *Metal Mater Trans A* 36(12):3427–3438

Christian JW, Mahajan S (1995) Deformation twinning. *Prog Mater Sci* 39:1–57

Cox MA, Cavosie AJ, Bland PA, Miljković K, Wingate MTD (2018) Microstructural dynamics of central uplifts: Reidite offset by zircon twins at the Woodleigh impact structure, Australia. *Geology* 46(11):983–986. <https://doi.org/10.1130/g45127.1>

Crow CA, Moser DE, McKeegan KD (2018) Shock metamorphic history of > 4 Ga Apollo 14 and 15 zircons. *Meteor Planet Sci* 15:8. <https://doi.org/10.1111/maps.13184>

Darling JR, Moser DE, Barker IR, Tait KT, Chamberlain KR, Schmitt AK, Hyde BC (2016) Variable microstructural response of baddeleyite to shock metamorphism in young basaltic shergottite NWA 5298 and improved U-Pb dating of Solar System events. *Earth Planet Sci Lett* 444:1–12. <https://doi.org/10.1016/j.epsl.2016.03.032>

Deer WA, Howie RA, Zussman J (1982) Rock-forming minerals: orthosilicates, Volume 1A, 2nd edn. Geological Society of London, London

Deutsch A, Schärer U (1990) Isotope systematics and shock-wave metamorphism: I. U-Pb in zircon, titanite and monazite, shocked experimentally up to 59 GPa. *Geochimica et Cosmochimica Acta* 54(12):3427–3434

Erickson TM, Cavosie AJ, Moser DE, Barker IR, Radovan HA (2013) Correlating planar microstructures in shocked zircon from the Vredefort Dome at multiple scales: crystallographic modeling, external and internal imaging, and EBSD structural analysis. *Am Miner* 98(1):53–65. <https://doi.org/10.2138/am.2013.4165>

Erickson TM, Pearce MA, Taylor RJM, Timms NE, Clark C, Reddy SM, Buick IS (2015) Deformed monazite yields high-temperature tectonic ages. *Geology* 43(5):383–386. <https://doi.org/10.1130/g36533.1>

Erickson TM, Cavosie AJ, Pearce MA, Timms NE, Reddy SM (2016) Empirical constraints on shock features in monazite using shocked zircon inclusions. *Geology* 44(8):635–638

Erickson TM, Pearce MA, Reddy SM, Timms NE, Cavosie AJ, Bourdet J, Rickard WDA, Nemchin AA (2017a) Microstructural constraints on the mechanisms of the transformation to reidite in naturally shocked zircon. *Contrib Miner Pet* 172(1):6

Erickson TM, Timms NE, Kirkland CL, Tohver E, Cavosie AJ, Pearce MA, Reddy SM (2017b) Shocked monazite chronometry: integrating microstructural and in situ isotopic age data for determining precise impact ages. *Contrib Miner Pet* 172(2–3):11. <https://doi.org/10.1007/s00410-017-1328-2>

Facchini A, Bruno E, Chiari G (1979) The structure of bytownite quenched from 1723 K. *Acta Crystallogr Sect B Struct Crystallogr Cryst Chem* 35(1):34–42

Farnan I, Balan E, Pickard CJ, Mauri F (2003) The effect of radiation damage on local structure in the crystalline fraction of $ZrSiO_4$: investigating the ^{29}Si NMR response to pressure in zircon and reidite. *Am Mineral* 88(11–12):1663–1667

Feignon J-G, Ferrière L, Koeberl C (2018) Petrography and shock metamorphism of granitoid samples from the Chicxulub peak-ring IODP-ICDP expedition 364 drill core. In: EGU General Assembly Conference Abstracts, p 20

Ferrière L, Rae ASP, Poelchau M, Koeberl C, the IODP-ICDP Expedition 364 Science Party (2017) Macro- and microscopic evidence of impact metamorphism in rocks from the Chicxulub peak ring IODP-ICDP Expedition 364 drill core. In: 48th Lunar and planetary science conference, vol., The Woodlands, Texas, p 1600

Frost BR, Chamberlain KR, Schumacher JC (2001) Spheine (titanite): phase relations and role as a geochronometer. *Chem Geol* 172(1–2):131–148

Grieve R, Therriault A (2000) Vredefort, Sudbury, Chicxulub: three of a kind? *Annu Rev Earth Planet Sci* 28(1):305–338

Güldemeister N, Wünnemann K, Durr N, Hiermaier S (2013) Propagation of impact-induced shock waves in porous sandstone using mesoscale modeling. *Meteor Planet Sci* 48(1):115–133. <https://doi.org/10.1111/j.1945-5100.2012.01430.x>

Gulick SP, Barton PJ, Christeson GL, Morgan JV, McDonald M, Mendoza-Cervantes K, Pearson ZF, Surendra A, Urrutia-Fucugauchi J, Vermeesch PM, Warner MR (2008) Importance of pre-impact crustal structure for the asymmetry of the Chicxulub impact crater. *Nat Geosci* 1(2):131–135

Gulick SPS, Christeson GL, Barton PJ, Grieve RAF, Morgan JV, Urrutia-Fucugauchi J (2013) Geophysical characterization of the Chicxulub impact crater. *Rev Geophys* 51(1):31–52. <https://doi.org/10.1002/rog.20007>

Gulick S, Morgan J, Mellett CL, Green SL, Bralower T, Chenot E, Christeson G, Claeys P, Cockell C, Coolen MJL, Ferrière L, Gebhardt C, Goto K, Jones H, Kring D, Lofi J, Lowery C, Ocampo-Torres R, Perez-Cruz L, Pickersgill AE, Poelchau M, Rae A, Rasmussen C, Rebolledo-Vieyra M, Riller U, Sato H, Smit J, Tikoo S, Tomioka N, Urrutia-Fucugauchi J, Whalen M, Wittmann A, Yamaguchi K, Xiao L, Zylberman W (2017) Expedition 364 summary. In: Morgan J, Gulick S, Mellett CL, Green SL, Scientists at E (eds) Proceedings of the international ocean discovery program, vol 364. College Station, TX (International Ocean Discovery Program), Texas, pp 1–23

Hayward PJ, Cecchetto EV (1982) Scientific Basis for Nuclear Waste Management. North Holland, Amsterdam

Hazen RM, Finger LW (1979) Crystal structure and compressibility of zircon at high pressure. *Am Mineral* 64:196–201

Hey MH (1982) International Mineralogical Association: commission on new minerals and mineral names. *Mineral Mag* 46(341):513–514

Higgins JB, Ribbe PH (1976) The crystal chemistry and space groups of natural and synthetic titanites. *Am Miner* 61(9–10):878–888

Hildebrand AR, Penfield GT, Kring DA, Pilkington M, Camargo ZA, Jacobsen SB, Boynton WV (1991) Chicxulub crater: a possible Cretaceous/Tertiary boundary impact crater on the Yucatan Peninsula, Mexico. *Geology* 19(9):867–871

Kirkland CL, Fougerouse D, Reddy SM, Hollis J, Saxe DW (2018) Assessing the mechanisms of common Pb incorporation into titanite. *Chem Geol* 483:558–566. <https://doi.org/10.1016/j.chemeo.2018.03.026>

Koeberl C, Reimold WU, Kracher A, Träxler B, Vormaier A, Körner W (1996) Mineralogical, petrological, and geochemical studies of drill core samples from the Manson impact structure, Iowa. *Geological Society of America Special Papers* 302(166)

Kunz M, Xirouchakis D, Lindsley DH, Hausermann D (1996) High-pressure phase transition in titanite ($CaTiOSiO_4$). *Am Miner* 81(11–12):1527–1530

Leroux H, Reimold WU, Koerberl C, Hornemann U, Doukan J-C (1999) Experimental shock deformation in zircon: a transmission electron microscopy study. *Earth Planet Sci Lett* 169:291–301

Morgan J, Warner M, Brittan J, Buffler R, Camargo A, Christeson G, Denton P, Hildebrand A, Hobbs R, Macintyre H, Mackenzie G (1997) Size and morphology of the Chicxulub impact crater. *Nature* 390(6659):472–476

Morgan JV, Gulick SP, Bralower T, Chenot E, Christeson G, Claeys P, Cockell C, Collins GS, Coolen MJ, Ferrière L, Gebhardt C (2016) The formation of peak rings in large impact craters. *Science* 354(6314):878–882

Morgan J, Gulick S, Mellett CL, Green SL, Expedition364Scientists (2017) Chicxulub: Drilling the K-Pg Impact Crater. Expedition 364 of the mission-specific drilling platform from and to Progresso, Mexico. Site M0077. In: Proceedings of the international ocean discovery program, p 364

Moser DE, Davis WJ, Reddy SM, Flemming RL, Hart RJ (2009) Zircon U-Pb strain chronometry reveals deep impact-triggered flow. *Earth Planet Sci Lett* 277(1–2):73–79. <https://doi.org/10.1016/j.epsl.2008.09.036>

Moser DE, Cupelli CL, Barker IR, Flowers RM, Bowman JR, Wooden J, Hart JR (2011) New zircon shock phenomena and their use for dating and reconstruction of large impact structures revealed by electron nanobeam (EBSD, CL, EDS) and isotopic U-Pb and (U-Th)/He analysis of the Vredefort dome. *Can J Earth Sci* 48(2):117–139. <https://doi.org/10.1139/e11-011>

Mügge O (1889) Über durch Druck entstandene Zwillinge von Titanit nach den Kanten [110] und [HO]., 11, 98. *Neues Jahrb Miner Geol u Paläontol* 11:98–115

Müller WF, Franz G (2004) Unusual deformation microstructures in garnet, titanite and clinzoisite from an eclogite of the Lower Schist Cover, Tauern Window, Austria. *Eur J Mineral* 16(6):939–944. <https://doi.org/10.1127/0935-1221/2004/0016-0939>

Nemchin A, Timms N, Pidgeon R, Geisler T, Reddy S, Meyer C (2009) Timing of crystallization of the lunar magma ocean constrained by the oldest zircon. *Nat Geosci* 2(2):133–136. <https://doi.org/10.1038/NGEO417>

O'Neill C, Marchi S, Zhang S, Bottke W (2017) Impact-driven subduction on the Hadean Earth. *Nat Geosci* 10(10):793–797. <https://doi.org/10.1038/ngeo3029>

Papapavlou K, Darling JR, Storey CD, Lightfoot PC, Moser DE, Lasalle S (2017) Dating shear zones with plastically deformed titanite: new insights into the orogenic evolution of the Sudbury impact structure (Ontario, Canada). *Precambr Res* 291:220–235. <https://doi.org/10.1016/j.precamres.2017.01.007>

Papapavlou K, Darling JR, Moser DE, Barker IR, White LF, Lightfoot PC, Storey CD, Dunlop J (2018) U-Pb isotopic dating of titanite microstructures: potential implications for the chronology and identification of large impact structures. *Contrib Miner Pet* 173:82. <https://doi.org/10.1007/s00410-018-1511-0>

Prince E, Donnay G, Martin RF (1973) Neutron diffraction refinement of an ordered orthoclase structure. *Am Miner* 58(5–6):500–507

Prior DJ, Boyle AP, Brenker F, Cheadle MC, Day A, Lopez G, Peruzzo L, Potts GJ, Reddy S, Spiess R, Timms NE, Trimby P, Wheeler J, Zetterström L (1999) The application of electron backscatter diffraction and orientation contrast imaging in the SEM to textural problems in rocks. *Am Miner* 84:1741–1759

Rae ASP (2018) The kinematics and dynamics of complex crater collapse. Imperial College London, London

Rae ASP, Morgan JVC, Collins GS, Grieve RAF, Osinski GR, Salge T, Hall B, Ferrière L, Poelchau M, Gulick SPS, the IODP-ICDP Expedition 364 Science Party (2017) Deformation, shock barometry, and porosity within shocked target rocks of the Chicxulub peak ring: results from IODP-ICDP expedition 364. In: 48th lunar and planetary science conference, vol., The Woodlands, Texas, p 1934

Reddy SM, Timms NE, Pantleon W, Trimby P (2007) Quantitative characterization of plastic deformation of zircon and geological implications. *Contrib Miner Pet* 153(6):625–645. <https://doi.org/10.1007/s00410-006-0174-4>

Reddy SM, Johnson TE, Fischer S, Rickard WDA, Taylor RJM (2015) Precambrian reidite discovered in shocked zircon from the Stac Fada impactite, Scotland. *Geology* 43(10):899–902. <https://doi.org/10.1130/g37066.1>

Renne PR, Deino ALHFJ, Kuiper KF, Mark DF, Mitchell WS, Morgan LE, Mundil R, Smit J (2013) Time scales of critical events around the Cretaceous-Paleogene boundary. *Science* 339(6120):684–687

Riller U, Poelchau MH, Rae ASP, Schulte FM, Collins GS, Melosh HJ, Grieve RAF, Morgan JV, Gulick SPS, Lofi J, Diaw A, McCall N, Kring DA, Party I-IES (2018) Rock fluidization during peak-ring formation of large impact structures. *Nature* 562(7728):511–518. <https://doi.org/10.1038/s41586-018-0607-z>

Salje E, Schmidt C, Bismayer U (1993) Structural phase transition in titanite, CaTiSiO_5 : a Raman spectroscopic study. *Phys Chem Miner* 19(7):502–506

Sands DE (1969) Introduction to crystallography. WA Benjamin, New York

Schmieder M, Kring DA, Lapan TJ, Gulick SPS, Stockli DF, Rasmussen C, Rae ASP, Ferrière L, Poelchau M, Xiao L, Wittmann A (2017) Sphene and TiO_2 assemblages in the Chicxulub peak ring: U-Pb systematics and implications for shock pressures, temperatures, and crater cooling. *Meteor Planet Sci* 52:A308–A308

Schulte P, Alegret L, Arenillas I, Arz JA, Barton PJ, Bown PR, Bralower TJ, Christeson GL, Claeys P, Cockell CS, Collins GS (2010) The Chicxulub asteroid impact and mass extinction at the Cretaceous-Paleogene boundary. *Science* 327(5970):1214–1218

Speer JA, Gibbs GV (1976) The crystal structure of synthetic titanite, CaTiOSiO_4 , and the domain textures of natural titanites. *Am Miner* 61(3–4):238–247

Taylor M, Brown GE (1976) High-temperature structural study of the $\text{P}_2/\text{a} <-\rightarrow \text{A}_2/\text{a}$ phase transition in synthetic titanite, CaTiSiO_5 . *Am Miner* 61(5–6):435–447

Thomson OA, Cavosie AJ, Moser DE, Barker I, Radovan HA, French BM (2014) Preservation of detrital shocked minerals derived from the Ga Sudbury impact structure in modern alluvium and Holocene glacial deposits. *Geol Soc Am Bull* 126(5–6):720–737. <https://doi.org/10.1130/b30958.1>

Timms NE, Reddy SM, Healy D, Nemchin AA, Grange ML, Pidgeon RT, Hart R (2012) Resolution of impact-related microstructures in lunar zircon: a shock-deformation mechanism map. *Meteor Planet Sci* 47(1):120–141. <https://doi.org/10.1111/j.1945-5100.2011.01316.x>

Timms NE, Erickson TM, Zanetti M, Pearce MA, Cayron C, Cavosie AJ, Reddy SM, Wittmann A, Carpenter PK (2017a) Cubic zirconia in $> 2370^\circ\text{C}$ impact melt records Earth's hottest crust. *Earth Planet Sci Lett* 477(1):52–58. <https://doi.org/10.1016/j.epsl.2017.08.012>

Timms NE, Erickson TM, Pearce MA, Cavosie AJ, Schmieder M, Tohver E, Reddy SM, Zanetti M, Nemchin AA, Wittmann A (2017b) A pressure-temperature phase diagram for zircon at extreme conditions. *Earth-Sci Rev* 165:185–202. <https://doi.org/10.1016/j.earscirev.2016.12.008>

Timms NE, Healy D, Erickson TM, Nemchin AA, Pearce MA, Cavosie AJ (2018) Role of elastic anisotropy in the development of deformation microstructures in zircon. In: Moser D, Corfu F, Reddy S, Darling J, Tait K (eds) Microstructural geochronology: planetary records down to atom scale, geophysical monograph, vol 232. AGU-Wiley, Hoboken, pp 183–202

Wechsler BA, Lindsley DH, Prewitt CT (1984) Crystal structure and cation distribution in titanomagnetites ($\text{Fe}_{3-x}\text{Ti}_x\text{O}_4$). *Am Miner* 69(7–8):754–770

Wheeler J, Prior D, Jiang Z, Spiess R, Trimby P (2001) The petrological significance of misorientations between grains. *Contrib Miner Pet* 141(1):109–124. <https://doi.org/10.1007/s004100000225>

Wheeler J, Mariani E, Piazolo S, Prior DJ, Trimby P, Drury MR (2009) The weighted Burgers vector: a new quantity for constraining dislocation densities and types using electron backscatter diffraction on 2D sections through crystalline materials. *J Microsc* 233(3):482–494

White LF, Darling JR, Moser DE, Cayron C, Barker I, Dunlop J, Tait KT (2018) Baddeleyite as a widespread and sensitive indicator of meteorite bombardment in planetary crusts. *Geology* 46(8):719–722. <https://doi.org/10.1130/g45008.1>

Whitney DL, Evans BW (2009) Abbreviations for names of rock-forming minerals. *Am Miner* 95(1):185–187. <https://doi.org/10.2138/am.2010.3371>

Wittmann A, Kenkemann T, Schmitt RT, Stöffler D (2006) Shock-metamorphosed zircon in terrestrial impact craters. *Meteor Planet Sci* 41(3):433–454

Zhao JW, Xiao L, Liu HS, Xiao ZY, Morgan J, Gulick S, Kring D, Claeys P, Riller U, Wittmann A, Ferrière L (2017) Shock metamorphic effects of the peak ring granites within the Chicxulub Crater. *Lunar Planet Sci Conf Proc* 48:1421

Publisher's Note Springer Nature remains neutral with regard to jurisdictional claims in published maps and institutional affiliations.

Affiliations

Nicholas E. Timms¹ · Mark A. Pearce² · Timmons M. Erickson^{1,3} · Aaron J. Cavosie¹ · Auriol S. P. Rae^{4,5} · John Wheeler⁶ · Axel Wittmann⁷ · Ludovic Ferrière⁸  · Michael H. Poelchau⁵ · Naotaka Tomioka⁹ · Gareth S. Collins⁴ · Sean P. S. Gulick¹⁰ · Cornelia Rasmussen¹⁰ · Joanna V. Morgan⁴ · IODP-ICDP Expedition 364 Scientists

¹ The Institute for Geoscience Research (TIGeR), Space Science and Technology Centre, School of Earth and Planetary Sciences, Curtin University, GPO Box U1987, Perth, WA 6845, Australia

² CSIRO Mineral Resources, Australian Resources Research Centre, 26 Dick Perry Avenue, Kensington, WA 6151, Australia

³ Jacobs-JETS, NASA Johnson Space Center, Astromaterials Research and Exploration Science Division, Mailcode XI3, 2101 NASA Parkway, Houston, TX 77058, USA

⁴ Department of Earth Science and Engineering, Imperial College London, London, UK

⁵ Institut für Geo- und Umweltnaturwissenschaften, Albert-Ludwigs-Universität, Freiburg, Albertstraße 23b, 79104 Freiburg, Germany

⁶ Department of Earth and Ocean Sciences, University of Liverpool, Liverpool L69 3GP, UK

⁷ Eyring Materials Center, Arizona State University, Tempe, AZ, USA

⁸ Natural History Museum, Burgring 7, 1010 Vienna, Austria

⁹ Kochi Institute for Core Sample Research, Japan Agency for Marine-Earth Science and Technology, Kochi, Japan

¹⁰ Institute for Geophysics and Department of Geological Sciences, Jackson School of Geosciences, University of Texas at Austin, Austin, TX, USA